

Chapter 2

Image Enhancement, Feature Extraction and Geospatial Analysis in an Archaeological Perspective

Rosa Lasaponara and Nicola Masini

Abstract The goal of image processing for archaeological applications is to enhance spatial patterns and/or local anomalies linked to ancient human activities and traces of palaeo-environments still fossilized in the modern landscape. In order to make the satellite data more meaningful for archaeologists and more exploitable for investigations, reliable data processing may be carried out. Over the years a great variety of digital image enhancement techniques have been devised for specific application fields according to data availability. Nevertheless, only recently these methods have captured great attention also in the field of archaeology for an easier extraction of quantitative information using effective and reliable semiautomatic data processing. The setting up of fully-automatic methodologies is a big challenge to be strategically addressed by research communities in the next years.

Keywords Radiometric and spectral enhancement • Spectral indices • PCA • TCT • Spatial enhancement • Fourier • Wavelet • Filtering • Geospatial analysis

2.1 Introduction

The application of aerial photographs had been long appreciated in archaeological investigations (see, for example, Reeves 1936; Miller 1957; Stone 1964; Estes et al. 1977; Spennemann 1987; Weber and Yool 1999; Bewley et al. 1999; Wilson 2000).

R. Lasaponara (✉)
Institute of Methodologies for Environmental Analysis, CNR-IMAA,
C. da S. Loya, 85100 Tito Scalo, PZ, Italy
e-mail: lasaponara@imaa.cnr.it

N. Masini
Institute of Archaeological and Architectural Heritage, CNR-IBAM,
C. da S. Loya, 85050 Tito Scalo, PZ, Italy
e-mail: n.masini@ibam.cnr.it

In fact, over the last century, aerial reconnaissance has been one of the most important ways in which new archaeological sites have been discovered throughout the world. The advantages of aerial photographs are manifold: they can be taken vertically or obliquely, easily interpreted, used for photogrammetric applications. They also provide a three-dimensional view.

Presently, the great amount of multispectral VHR satellite images, even available free of charge in Google earth (see, for example, Beck 2006; Brown et al. 2011; Kennedy and Bishop 2011) opened new strategic challenges in the field of remote sensing in archaeology (Campana and Forte 2006; Parcak 2009; Lasaponara and Masini 2011; Giardino 2011). These challenges substantially deal with: (i) the strategic exploitation of both aerial and satellite data as much as possible, (ii) the setting up of effective and reliable automatic and/or semiautomatic data processing strategies and (iii) the integration with other data sources from documentary resources to the traditional ground truthing activity including geophysical prospection.

VHR satellites provide high resolution data which can improve knowledge on past human activities providing precious qualitative and quantitative information developed to such an extent that currently they share many of the physical characteristics of aerial imagery. This makes them ideal for investigations ranging from a local to a regional scale (see, for example, Urwin and Ireland 1992; Sussman et al. 1994; Stein and Cullen 1994; Clark et al. 1998; Fowler 1996; Fritz 1996; Drake 1997; Strahler and Strahler 1997; Sever 1998; Sheets and Sever 1988; Sarris and Jones 2000; Toutin 2001, 2002; Kouchoukos 2001; Davis and Wang 2003; Lasaponara and Masini 2006a, b, 2007a, 2011; Masini and Lasaponara 2006, 2007). Moreover, satellite data are still the only data source for research performed in areas where aerial photography is restricted because of military or political reasons. Among the main advantages of using satellite remote sensing compared to traditional field archaeology herein we briefly summarized the following:

- (a) **Multiscale/Multispectral capability.** Satellite remote sensing provides panchromatic and multispectral images acquired simultaneously at different scales and resolutions for the study area. This allows us to perform inter-site and intra-site analysis, ranging from detailed archaeological investigations to regional environmental and landscape studies.
- (b) **High temporal resolution.** Satellite remote sensing assures the acquisition of imagery at high repeated re-visit cycle (1–3 days for VHR), thus allowing the possibility of performing multitemporal observations useful for systematic risk monitoring and for revealing changes over time.
- (c) **Non-invasivity.** Remote sensing enables us to detect unknown sites and study the structure and distribution of ancient remains without exposing them, saving money, time and maintaining archaeological relics “as they are” thus preserving them for additional future investigations.
- (d) **Data manipulation and information extraction.** Data manipulation enables the enhancement and extraction of features, patterns and their recognition, thus providing improved information on cultural heritage.

Among all the data manipulation techniques, image enhancement can make subtle features more visible to the human eye and, therefore, easier to interpret than raw data and fruitfully manageable for further data processing.

The choice of particular digital image enhancement approaches, among the great number of today's available techniques, depends on the application, data availability, experience and preferences of the image analyst (Richards and Jia 2006). It is really important to highlight that the image enhancement algorithms are data set and application-dependent, therefore, their performance can strongly vary from one application to another or from one data set to another.

We can categorize the image enhancement approaches into three main groups:

- Radiometric enhancement based on the values of individual pixels;
- Spectral enhancement based on the transformation of the values of each pixel on a multi-band basis;
- Spatial enhancement techniques based on the values of individual given pixels and their neighboring areas.

Moreover the enhancement may be carried out on: (i) temporary mode, when an image is only displayed in a viewer and all edits are not saved; or (ii) permanent mode, when all operations are saved as another image file.

2.2 Radiometric Enhancement

The radiometric enhancement techniques are based on the values of individual pixels within each band. To emphasize targets/objects/features of interest, these techniques are based on the use of histograms, namely the graph of the number of pixels with a given brightness versus brightness values. The histogram provides a discrete probability distribution being that the relative height of a given bar indicates the chance to find a pixel in the image with that particular brightness value, generally called the Digital Number (DN). The histogram based analysis is very useful since the tonal or radiometric quality of an image can be assessed from its histogram (see in Fig. 2.1 the histogram of a study area in Cauchy in Peru).

Pixels related to different materials may have similar brightness values. This is because different materials or objects may reflect or emit similar amounts of radiant flux. In this condition, it is highly probable to have an image with a poor contrast, which can be enhanced by stretching the image data to re-arrange the brightness values and obtain a new histogram over the full available range. Contrast enhancement is only intended to improve the visual quality of an image by using the whole available radiometric range (usually 0–255). It does not change the pixel values, unless it is saved as a new image. Contrast enhancement is very helpful for

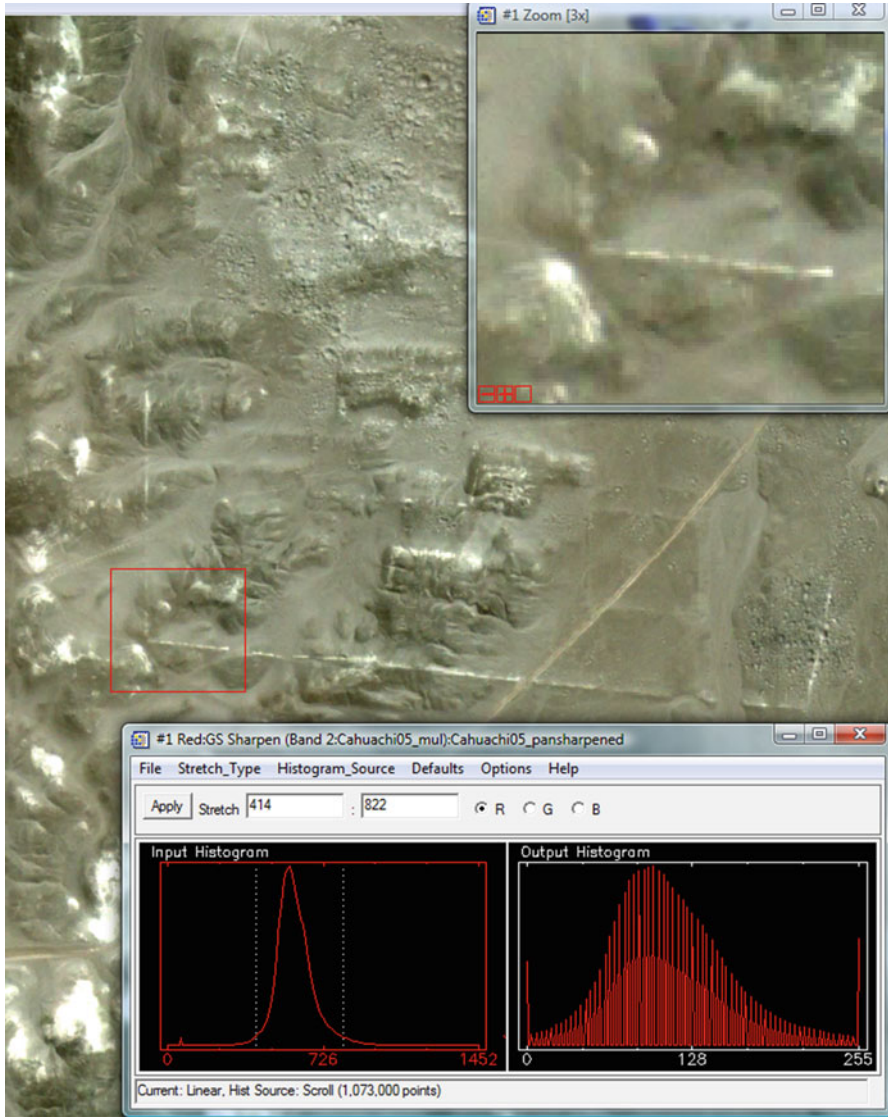


Fig. 2.1 Histogram of QuickBird (2005 March) *red* channel of a subset related to the *square block* in the upper right which includes a portion of the enclosure of a sacred area in the Ceremonial Centre of Cahuachi (Peru)

sharpening subtle details, but it is not a good practice to use the saved image for classification and/or change detection, etc.

Several contrast enhancement techniques are frequently used in archaeology (see for example Beck et al. 2007; Campana 2004; Campana and Francovich 2003) and implemented in common image processing routines and in open-source

softwares. A comprehensive analysis is in Richards and Jia (2006), herein we only outline some of them below:

- Linear techniques:
 - Minimum-maximum contrast stretch (including percentage or standard deviation);
 - Piecewise linear contrast stretch.
- Non-linear techniques:
 - Histogram equalization;
 - Logarithmic and Exponential Contrast Enhancement.

2.2.1 Linear Enhancement Techniques

The minimum-maximum contrast is expressed by the following mathematical formulation.

$$BV_{out} = \frac{(BV_{in} - \min_k)}{(\max_k - \min_k)} \text{quant} \quad (2.1)$$

where:

- BV_{out} is the output brightness value,
- BV_{in} is the original input brightness value,
- \min_k is the minimum value in the image,
- \max_k is the maximum value in the image, and
- quant_k is the range of the brightness values that can be displayed (generally 255)

The linear contrast stretching with percentage or standard deviation defines a given percentage at the top or low values (generally 2% or 5% and similarly in $\pm 1\sigma$, $\pm 2\sigma$, $\pm 3\sigma$), of the image that will be set to 0 or 255; whereas the rest of the values are linearly stretched. It is also possible to apply a piecewise linear contrast stretch with specified break points, as shown in Fig. 2.2, to flexibly fit the non-Gaussian histograms (i.e. bimodal, trimodal). The user can also generally specify the number of break points.

2.2.2 Non Linear Enhancement Techniques

One of the most common non linear enhancement techniques is the Histogram equalization. Dark and light features can be easily enhanced by using logarithmic and exponential contrast stretch, respectively.

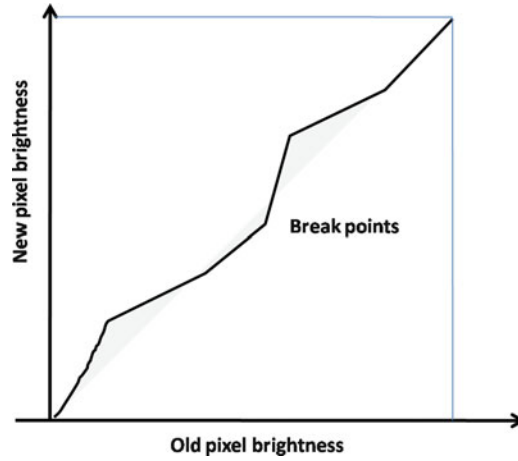


Fig. 2.2 Linear contrast stretch with specified break points

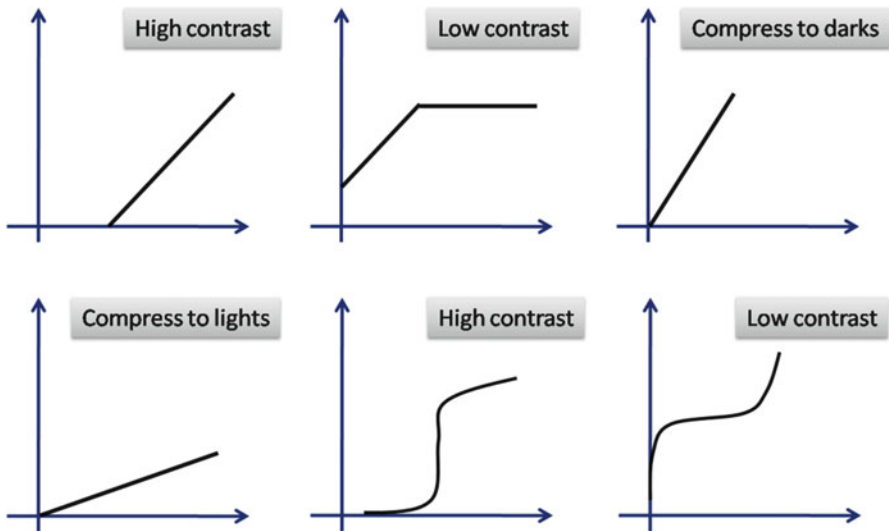


Fig. 2.3 Examples of histogram equalization functions

Figure 2.3 shows some examples of functions. Figure 2.4 depicts the results from linear and equalization enhancement for an archaeological site.

According to the mathematical formulation, the output values are generally scaled to lie within the range of the device used to display the image and that the output values are rounded to allow discrete values.

Please note that contrast modification simply locates the new histogram at different locations without altering size and number of bars of the old histogram.

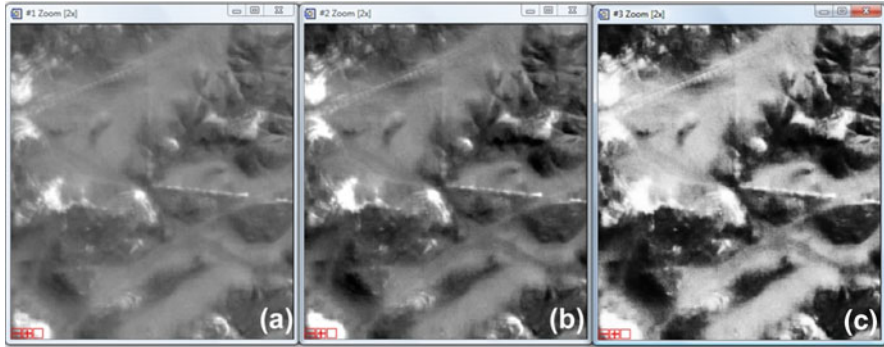


Fig. 2.4 (a) Same subset as in Fig. 2.2. (b–c) Results from linear and equalization enhancement, respectively. The latter emphasize the contrast between the linear features and its surrounding

2.2.3 Red-Green-Blue Colour Composites

The use of colour composites can facilitate the interpretation of multi-channel images by exploiting the fact that the visual overlapping of three images enhances the different types of surface/features/objects characterized by different grey levels in the three bands. The possibilities of varying the number of colour compositions are linked directly to the number of available spectral channels being the number of the mathematical combinations of them. In particular, the RGB (Red-Green-Blue Colour Composites) provides color visualization very close to the human colour perception and this can make the identification of different types of information easier. Figure 2.5 shows the result from RGB Composites. The Colour Composites visualization can be employed in conjunction with a Lookup- Table (LUT) used to transform the input data into a more interpretable output format. For example, a greyscale picture of the sea and land will be transformed into a colour image to emphasize the differences in the surfaces.

The RGB can be used not only for visualization but it may also be saved as a new image in a jpg file format. Moreover, slice may provide a more efficient distribution of the available 0–255 grey values to the range of the data. The RGB composition as well as false colour composition is widely used in archaeology (Aminzadeh and Samani 2006; Lasaponara et al. 2008; Alexakis et al. 2009). See for example, Fig. 2.6a, b which show two RGB compositions of ASTER images depicting the drainage basin of the Rio Nasca. They are the composition result of bands 3-2-1 (NIR/Red/Green channels) and bands 6-3-2 (SWIR/NIR/Red), respectively. In the false colour of Fig. 2.6b it is worth to note the red pixels which put in evidence a high reflectance of SWIR, related to a higher moisture content of the river and the tributaries respect to the surrounding arid area (for additional information on this case study the reader is referred to Chap. 12).

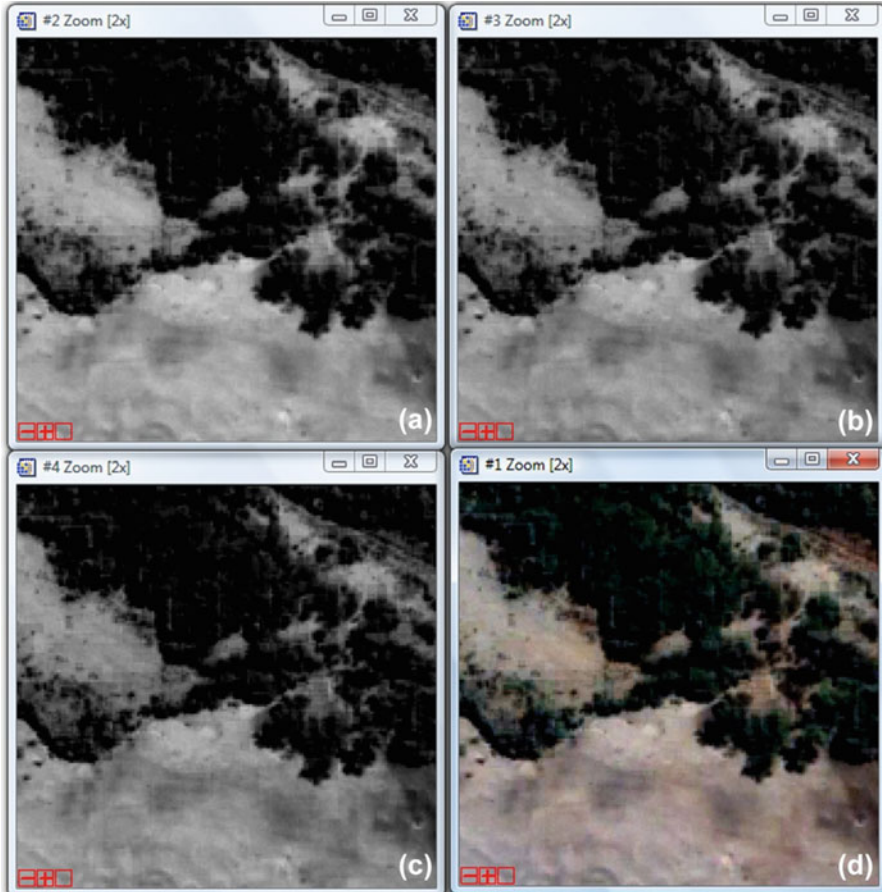


Fig. 2.5 Subset of a QuickBird image (2005 March) of Cahuachi. (a) Red band; (b) Green band; (c) Blue band; (d) RGB composition of the three bands Red-Green-Blue

2.3 Spectral Enhancement

2.3.1 Spectral Behaviour of Archaeological Marks

In order to exploit the multispectral capability of satellite imagery for the identification of archaeological marks all the available spectral bands (from visible to short wave infrared) may be considered.

Additionally, on the basis of multispectral properties of satellite remotely sensed data, archaeological-marks (crop or weed-marks) can be successfully identified by exploiting spectral indices that are mathematical combinations of different bands. Such indices are quantitative measures, based on the vegetation/soil/snow spectral properties that attempt to enhance the target under investigation.

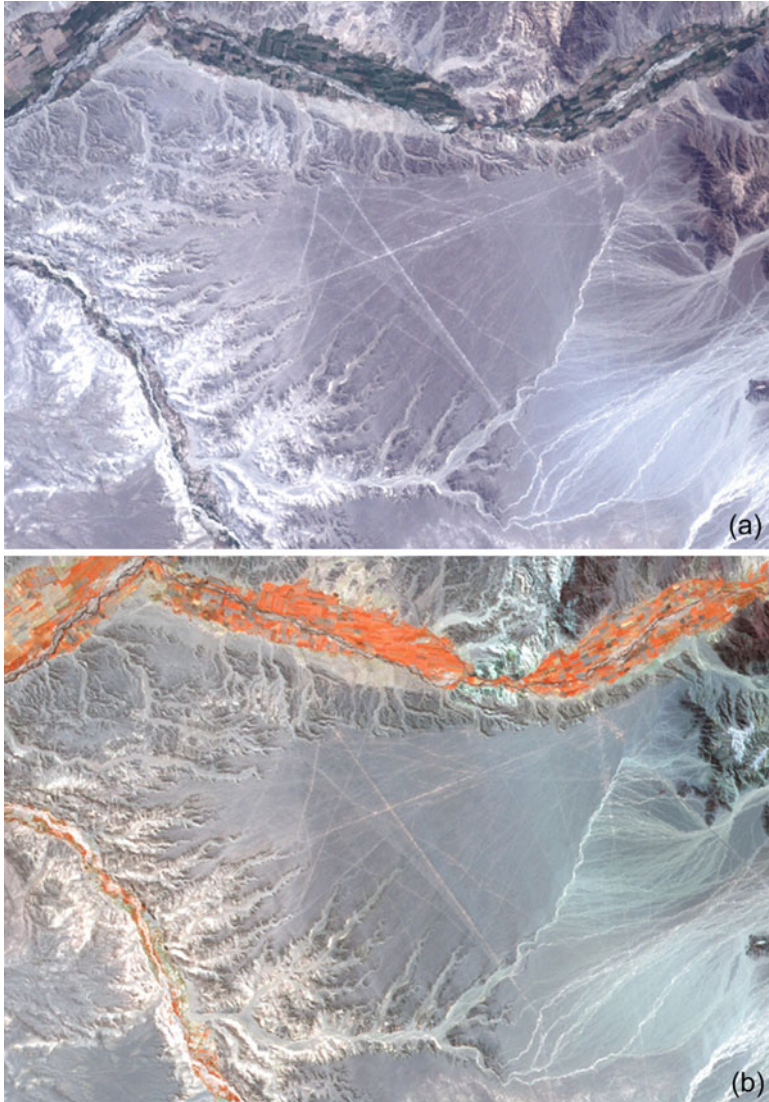


Fig. 2.6 ASTER images of the drainage Basin of the Rio Nasca. (a) RGB composition of bands 3-2-1 (NIR/Red/Green channels) and (b) bands 6-3-2 (SWIR/NIR/Red)

It is expected that, as in the case of aerial photos, satellite images at high spatial resolution should be able to identify the typical archaeological marks due the presence of buried structures. Recently, some evaluations concerning the capability of VHR satellite (QuickBird) spectral channels for archaeological applications

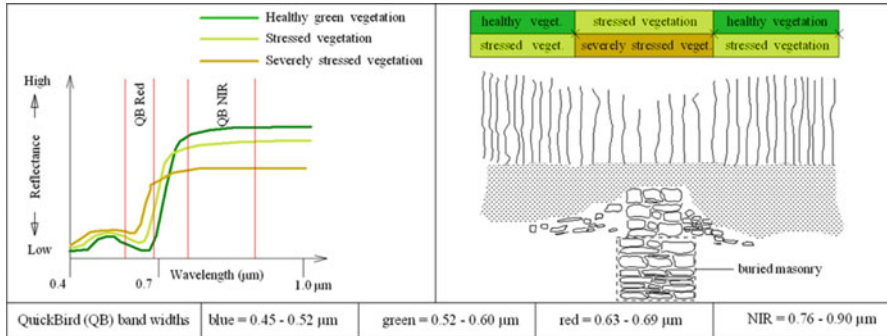


Fig. 2.7 Phenological and spectral characteristics linked to the presence of crop-marks. In the lower part of figure the QuickBird spectral range are reported

were performed (Lasaponara and Masini 2007a, b; Masini and Lasaponara 2007; Grøn et al. 2011). These investigations pointed out that the use of the

- (i) red channel enhances the shadow and soil marks
- (ii) NIR channel makes the detection of crop-marks easier

This is due to the fact that the presence of archaeological deposits under bare surface, lacking in vegetation, can influence the soil constituents and, above all, the moisture content. This causes a different spectral response of the Red band that can be used for the identification and spatial characterization of buried structures. Moreover, archaeological remains under vegetated surfaces strongly influence the state of plants, enhancing or reducing their growth. These subtle effects are only evident from an aerial view. The small differences in the plant growth and/or colour can be characterized by different spectral responses that, on the basis of VHR satellite spectral images, are enhanced in the NIR channel. Green and healthy plants tend to exhibit high NIR reflectance values; whereas vegetation under stress, due to lack of water or nutrients, is characterized by low NIR reflectance values.

As an example, yellow and brown curves, drawn in the left part of Fig. 2.7, are related to stressed and severely stressed plants, respectively. The Red and NIR bands are indicated by vertical red lines; thus, showing that the NIR offers a larger spectral separability than the Red band. This should make the NIR band ideal for identifying archaeological crop-marks linked to variations in vegetation growth and/or colour in comparison to the surrounding area (see, right part of Fig. 2.7).

For HR satellite data, SWIR bands are also available. SWIR spectral range is strongly sensitive to moisture content (soil moisture and leaf water content), thus allowing us to analyze moisture variations in space and time which are very useful for palaeo-geographic studies (see Chaps. 9, 11 and 12 in this book).

2.3.2 Spectral Indices

On the basis of remotely-sensed data, crop marks may be suitably identified by exploiting vegetation indices that are spectral combinations of different bands.

Such indices are quantitative measures, based on vegetation spectral properties that attempt to quantify biomass or vegetative vigor. The rationale for spectral vegetation indices is to exploit the spectral signatures of green and healthy vegetation as compared to those of stressed/unhealthy vegetation and other earth materials. Earth materials, such as, bare soil, sand, exposed rock, concrete, asphalt generally exhibit a steady rise in reflectance, without strong variations in the visible to the near-infrared. Whereas, green vegetation exhibits an increasing spectral reflectance from the visible to the near-infrared. Vegetation reflectance is very low in the blue and red regions, tends to be slightly higher in the green band and, finally, shows the greatest spectral response in the near-infrared (NIR).

Vegetation indices are spectral combinations of two or more bands devised to enhance the spectral signal of vegetation, mainly derived Red and near-infrared bands. For this reason they should allow a more reliable evaluation of photosynthetic activity and structural variations of the vegetation cover.

Vegetation indices operate by contrasting intense chlorophyll pigment absorption in the red with the high NIR reflectance of leaf mesophyll. The simplest form of vegetation index is the ratio between two digital values from the red and near-infrared spectral bands. The most widely used index is the well-known Normalized Difference Vegetation Index (NDVI) obtained by using the following formula:

$$\text{NDVI} = \frac{(\text{NIR} - \text{RED})}{(\text{NIR} + \text{RED})} \quad (2.2)$$

The arithmetic combination of the NDVI enables us to exploit the different spectral response of vegetation cover in the visible spectral (red) and near infrared bands. It provides a dimensionless numerical value. The formula is designed as a ratio, in order to normalize its variability field between -1 and $+1$, and in particular takes on NDVI values less than 0 for water, slightly higher than 0 for soils and between 0.4 and 0.7 for vegetation, dense vegetation can exceed 0.8 and be close to saturation (1) for a rainforest.

The normalization of the NDVI reduces the effects of variations caused by atmospheric contaminations. NDVI is indicative of plant photosynthetic activity and has been found to be related to the green leaf area index and the fraction of photosynthetically active radiation absorbed by vegetation. High (low) values of the vegetation index identify pixels covered by substantial proportions of healthy (disease or stressed) vegetation. It is expected that crop-marks created by vegetation patterns should be emphasized by using NDVI.

The NDVI (see Eq. 2.2) is able to account for vegetation vigor, and therefore, to detect the deterioration in pigments and leaf structure caused by the presence of subsurface archaeological materials. Figure 2.8 show the red, NIR and NDVI map for some archaeological areas.

NDVI has been firstly applied by Lasaponara and Masini (2006b) for enhancing crop marks in a medieval settlement, thus allowing to reconstruct its urban fabric.

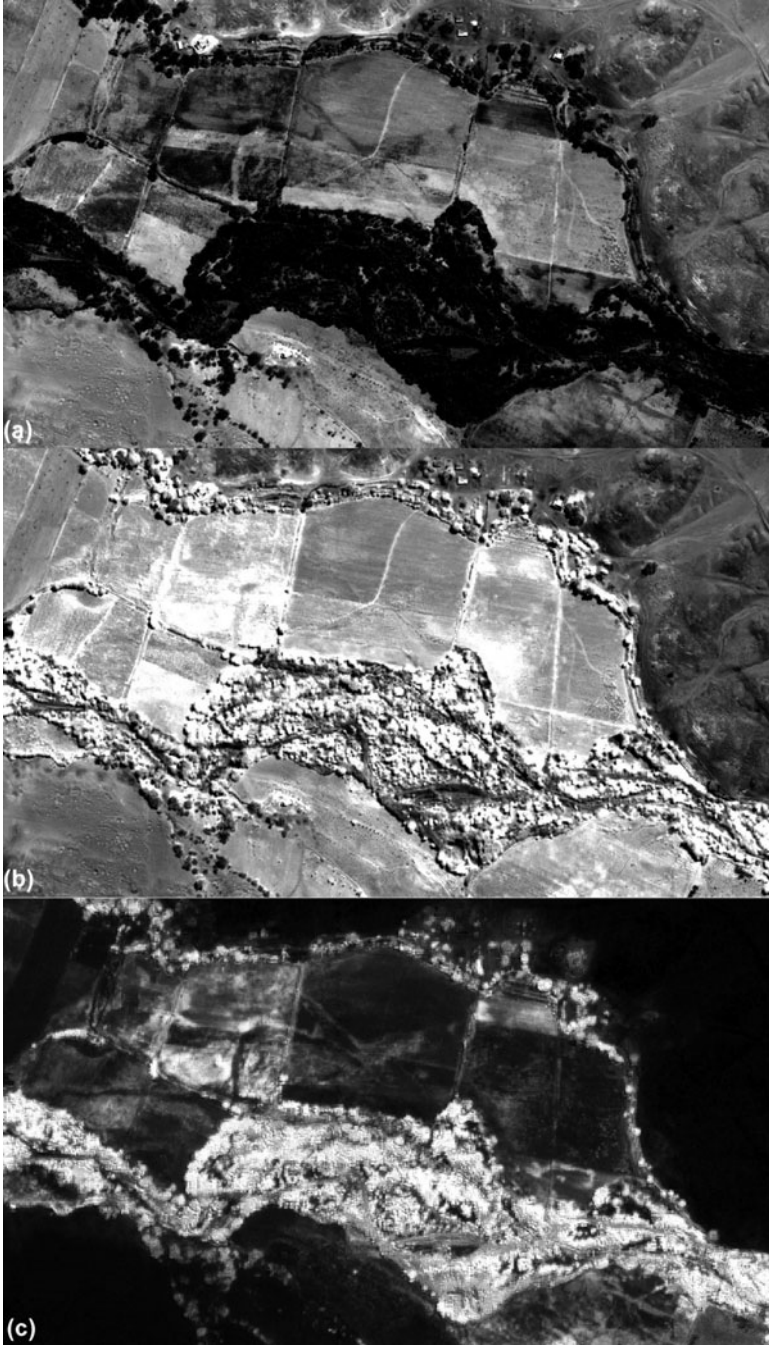


Fig. 2.8 QuickBird of Rio Nasca (2005 March). (a) Red band; (b) NIR band; (c) NDVI map

Other spectral bands and/or spectral combinations may be suitable for the enhancement of archaeological marks, single channels and spectral indices useful/or specifically designed for surface characterization (vegetation, soil, snow) can be considered for the analysis.

Spectral combinations of different bands are widely used since they generally tend to emphasize the spectral features caused by moisture content, the presence/type/status of vegetation cover, as well as by soil types and characteristics. Although the NDVI has been one of the most widely used vegetation indices, further spectral combinations were proposed to increase the sensitivity over a wide range of vegetation conditions and to reduce soil background influence and residual atmospheric contamination.

Among all the spectral indices devised over the years, we cite (i) albedo (Saunders 1990), Simple Ratio (SR), GEMI (Pinty and Verstraete 1992), SAVI (Huete 1988), Enhanced Vegetation Index (EVI), ARVI, Green NDVI, moisture index and snow index. Quite recently, the potentiality of using satellite SWIR spectral bands for moisture content estimation has been investigated.

Albedo is an indicator of the surface characteristics including brightness and darkness. The empirical approximation of surface albedo generally used is shown in formula 2.2 (Saunders 1990).

$$\text{Albedo} = (\text{NIR} + \text{RED})/2 \quad (2.3)$$

The simple ratio SR (see formula 2.4) is calculated using the ratio between NIR and red (or between NIR and Visible if no red band is available). Therefore, if these bands have the same or similar reflectance, the SR is 1 or close to 1. SR values for bare soils generally are near 1. When, for a given pixel, the amount of green vegetation increases the SR increases. Very high SR values are generally around 30.

$$\text{SR} = \text{NIR}/\text{RED} \quad (2.4)$$

Gitelson et al. (1996) proposed the use of a green channel instead of the red one for the remote sensing of vegetation. They devised the “Green”NDVI (see Eq. 2.5) that was applied to MODIS data and was found to be more sensitive to concentration in chlorophyll.

$$\text{Green NDVI} = \frac{(\text{NIR} - \text{GREEN})}{(\text{NIR} + \text{GREEN})} \quad (2.5)$$

The “Green”NDVI exhibits a wider range values than the original NDVI and is, on average, at least five times more sensitive to chlorophyll concentration.

In order to reduce the soil background influence, the soil-adjusted vegetation index (SAVI) was proposed by Huete (1988). This index is computed by using the red and near-infrared reflectance with some added terms (see Eq. 2.6). SAVI should be able to optimize the NDVI on the basis of Beer’s law.

$$SAVI = \frac{(1 + L) \cdot (NIR - RED)}{(NIR + RED + L)} \quad (2.6)$$

Where the term L can vary from 0 to 1 depending on the amount of visible soil; $L = 1$ is generally used when the amount of soil is unknown.

The SAVI is not sensitive to soil noise within a certain range of (Leaf Area Index) LAI values. The perfect range depends on the choice of the “ L ” value in the SAVI formulation. The authors suggested that, over the full range of canopy covers, $L = 0.5$ can be considered to be the optimal adjustment factor in reducing soil noise. Finally, the multiplication factor $(1 + L)$ is used to maintain the dynamic range of the index.

In order to minimize the influence of atmospheric effects Pinty and Verstraete (1992) proposed formula 2.7:

$$GEMI = \gamma \times (1 - 0.25\gamma) - \frac{(RED - 0.25)}{(1 - RED)} \quad (2.7)$$

Where

$$\gamma = \frac{(2 \times (NIR - RED) + 1.5 \times NIR + 0.5 \times RED)}{(NIR + RED + 0.5)}$$

The GEMI should be transparent to the atmosphere. It represents plant biological information similar to the NDVI. The main problem that is encountered with this index is mainly due to its complex formulation.

In order to reduce aerosol effects, the atmospheric resistant vegetation index (ARVI) was devised by Kaufman and Tanrer (1992).

This index is computed using formula 2.8. It is based on a function that should stabilize the index when there are temporal/spatial variations in the concentration of sand, gaseous, and particulate pollutants.

$$ARVI = \frac{(NIR - RB)}{(NIR + RB)} \quad (2.8)$$

where RB is a combination of the reflectances in the BLUE and in the RED channels: $RB = RED - \gamma \times (BLUE - RED)$ and γ depends on the aerosol type.

In order to optimize the vegetation signal from deserts to rainforests, the enhanced vegetation index (EVI) was developed.

It is obtained using formula 2.9.

$$EVI = \frac{(1 + L) \times (NIR - RED)}{(NIR + C_1 \times RED - C_2 \times BLUE + L)} \quad (2.9)$$

Where C_1 , C_2 , and L are constants empirically determined. The values generally used are as $C_1 = 6.0$; $C_2 = 7.5$; and $L = 1$.

The coefficient L denotes the canopy background and snow correction caused by differential NIR and red radiant transfer (transmittance) through a canopy; C_1 and C_2 denote the coefficient of the aerosol “resistance” term, which uses the blue band to correct for aerosol effects in the red band (Kaufman and Tanrer 1992). Therefore, the use of EVI should considerably reduce aerosol variations via the self-correcting combination of the red and blue channels.

Increased sensitivity should be achieved by placing more weight to the NIR reflectance component of the EVI formulation (see Eq. 2.9). Thus, allowing the EVI improved vegetation studies for densely vegetated areas as well as sparsely vegetated, arid and semi arid regions.

Recently, a number of satellite sensors at medium resolution (15–90 m) offer SWIR band acquisition which is quite sensitive to moisture content and moisture variation in both soil and vegetation cover. This capability has been supported by both modelling (Ceccato et al. 2001; Fourty and Baret 1998; Tucker 1980; Ustin et al. 1998; Zarco-Tejada et al. 2003) and experimental studies based on the available multispectral satellite datasets (Ceccato et al. 2002a, b; Chen et al. 2003; Jackson et al. 2004).

Actually, for more than three decades the NDVI (see formula 2.2) has been used as a surrogate to estimate vegetation water content even with strong limitations mainly encountered when vegetation coverage is dense and the index is close to the saturation level.

NDVI provides information closer to the amount and greenness of vegetation rather than moisture content and it is generally limited by soil reflection.

Using multispectral satellite data the estimation of moisture content in soil and vegetation may be improved using vegetation indices based upon NIR and SWIR and in general on the longer wave-lengths (1,240–3,000 nm), for example, the short-wave infrared (SWIR) reflectance (1,300–2,500 nm).

Several spectral indices, such as Normalized Vegetation Moisture Index (NVMI) or Normalized Difference Water Index (NDWI), mainly based on SWIR bands, can be computed to estimate moisture content for both soil and vegetation (see for example Fig. 2.9). The mathematical formulation of these indices (see formula 2.2 and 2.3) is very similar to the NDVI, but based on specific bands related to water absorption.

$$\text{NVMI} = \frac{(\text{NIR} - \text{SWIR})}{(\text{NIR} + \text{SWIR})} \quad (2.10)$$

$$\text{NDWI} = \frac{(\text{RED} - \text{SWIR})}{(\text{RED} + \text{SWIR})} \quad (2.11)$$

Both of these indices, NVMI and NDWI, are sensitive to water content in vegetation and soil, respectively being that the absorption of water content of

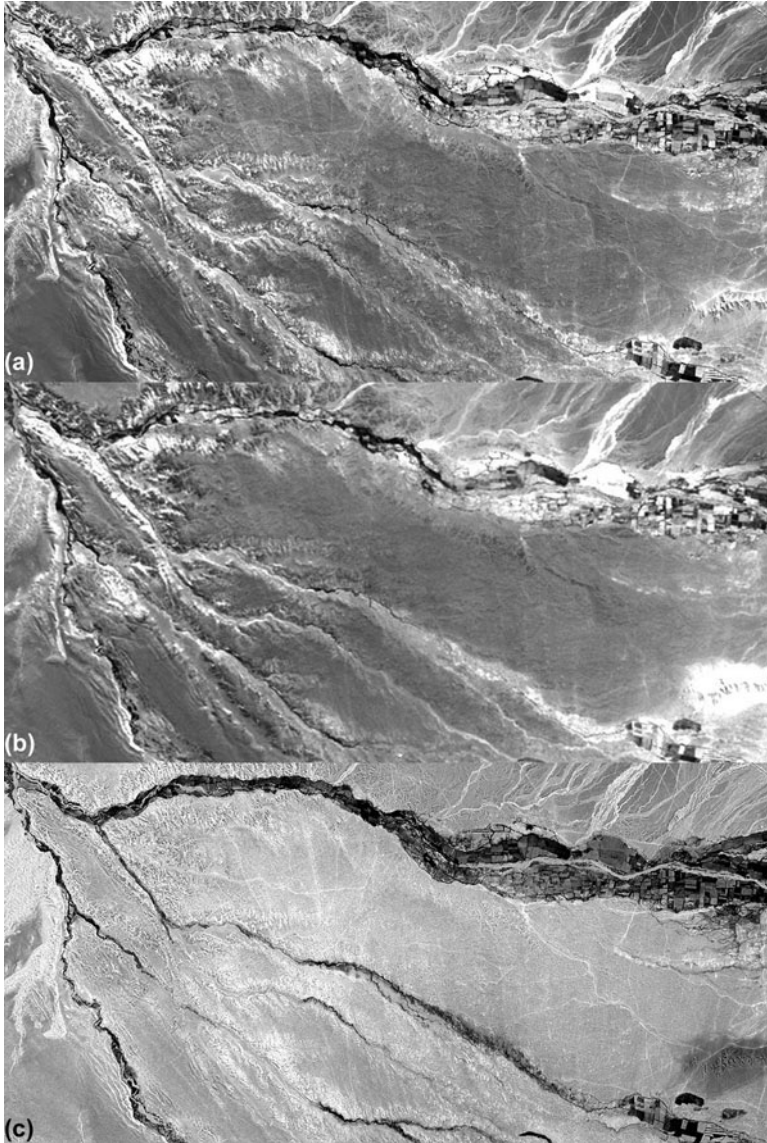


Fig. 2.9 ASTER images (2003 June) of the Rio Nasca drainage basin. (a) Red channel (band 2), (b) SWIR channel (band 6); (c) NDWI map

vegetation is negligible close to the NIR band (or close to the red band for soil), whereas a small absorption is present in the SWIR range.

Moreover, in comparison with NDVI, both NVMI and NDWI are less sensitive to the effects of the atmosphere, but effects of soil reflection are still present.

To date, there are two main satellite sensors which offer information in the SWIR spectral bands from medium to low spatial resolution, they are (i) Landsat MSS (available at 80 m), Landsat TM/ETM (available at 30 m) and (iii) ASTER images (with a spatial resolution ranging from 15 to 90 m).

Furthermore, in order to estimate the spectral separability (see Sect. 2.2) of all the considered spectral indicators, a sensitive analysis can be performed using an objective image quality index. This index can automatically predict perceived image quality.

As a whole, we can argue that the question is to assess which of the available vegetation indices, namely spectral indicators, is more suitable and adequate for the identification of the given archaeological marks (crop, soil, snow marks).

2.3.3 Spectral Separability of Vegetation Indices

In order to quantitatively assess the performance obtained from different vegetation indices we can use a universal quality index. This index, computed using formula 2.11, combines the correlation coefficient with luminance and contrast distortion (Wang and Bovik 2002). It was devised for image fusion to assess the quality of output image, as well as for image processing systems and algorithms. The quality index can be applied to qualitatively evaluate the capability of each satellite based index to enhance archaeological marks.

$$Q = \frac{(2 \times \mu_x \times \mu_y) \times (2 \times \sigma_{xy} + C_2)}{(\mu_x^2 + \mu_y^2 + C_1) \times (\sigma_x^2 + \sigma_y^2 + C_2)} \quad (2.12)$$

where $C_1 = (k_1 \times L)^2$ and $C_2 = (k_2 \times L)^2$.

σ_{xy} is the covariance between the two images x and y , σ_x and σ_y are the standard deviations, μ_x and μ_y are the means. L is the dynamic range for the image pixel values, $k_1 \ll 1$ and $k_2 \ll 1$ are two constants chosen equal to 0.01 and 0.03, respectively. Although the values selected for k_1 and k_2 are arbitrary, It was experienced that the quality index is insensitive to variations of k_1 and k_2 . Note that C_1 and C_2 are solely introduced to stabilize the measure. In other word, just to avoid the denominator approaches zero values for flat regions.

The quality index compares two images by using three parameters: luminance, contrast and structure. Note that Q is scaled between -1 and 1 . The value 1 is achieved when the two images x and y are the same. To account for local variation, a moving window sized 8×8 pixels was suggested by the Wang and Bovik (2002).

To measure the overall image quality the mean quality index can be rewritten as a three factor product, that can be regarded are relatively independent.

$$\begin{aligned}
 Q(x, y) &= f(l(x, y), c(x, y), s(x, y)) \\
 &= \frac{(\sigma_{xy} + \frac{C_2}{2}) \times (2 \times \mu_x \mu_y + C_1) \times 2 \times (\sigma_x \sigma_y + C_2)}{(\sigma_x \sigma_y \frac{C_2}{2}) \times (\mu_x^2 + \mu_y^2 + C_1) \times 2 \times (\sigma_x^2 + \sigma_y^2 + C_2)} \quad (2.13)
 \end{aligned}$$

In particular, among the three factor of Eq. 2.13, the first (varying between -1 and 1) represents the correlation coefficient between the two image x and y ; the second (varying between 0 and 1) measures the similarity between the mean luminance values of x and y and finally, the third (varying between 0 and 1) measures the contrast similarity.

Since traditionally the archaeological crop-mark identification has been performed by using black and white aerial photos, the performance evaluation may be performed comparing satellite panchromatic image with each considered multispectral index.

Of course other spectral separability indices may be considered, for any additional information reader is referred to Chap. 3 and references therein quoted.

2.3.4 Spectral Combinations Based on Linear Transformation

2.3.4.1 Tasseled Cap Transformation

Tasseled Cap Transformation (TCT) could be adopted for extracting archaeological features linked to ancient human transformations of landscape. Several authors have successfully applied TCT In archaeological studies, see, for example, Sarris and Jones (2000), Beck et al. (2007), Lasaponara and Masini (2007b). The TCT, also known as Kauth-Thomas technique, was devised for enhancing spectral information content of satellite data. The reader is referred to Crist and Kauth (1986) for an introduction.

The TCT is a linear affine transformation substantially based on the conversion of given input channel data set (or cartesian reference system) in a new data set (or cartesian reference system) of composite values; i.e., obtained via weighted sums of the input channels. The TCT is performed on a pixel basis (by using formula 2.14) to better show the underlying structure of the image.

$$TC = W_{TC}DN + B \quad (2.14)$$

where TC is the W_{TC} specific transformation (coefficients), DN Digital Number and B Bias.

The transformation W_{TC} depends on the considered sensor, because different sensors have different numbers of bands which, in turn have different spectral responses.

The original TCT was derived (Kauth and Thomas 1976) for the four bands of the Landsat MSS sensor. Later, the TCT was extended to the Landsat TM (Crist and Cicone 1984), ETM (as available in a routine of PCI Geomatics) and IKONOS sensor (Horne 2003).

All the existing TCTs decorrelate the multispectral data by using weighted sums of the input channels to extract a greater amount of information that can allow an easier identification of distinct surface types.

There are just three composite variables of TCT bands (axes) which are traditionally used:

- TCT-band 1 (brightness, measure of soil)
- TCT-band 2 (greenness, measure of vegetation)
- TCT-band 3 (wetness, interrelationship of soil and canopy moisture)

The weighted sums adapted from the ETM input channels:

$$TCT_{ETM-band1} = 0.1544 BLU + 0.2552 GREEN + 0.3592 RED + 0.5494 NIR \quad (2.15)$$

$$TCT_{ETM-band2} = -0.1099 BLU - 0.1255 GREEN - 0.2866 RED + 0.8226 NIR \quad (2.16)$$

$$TCT_{ETM-band3} = 0.3191 BLU + 0.5061 GREEN + 0.5534 RED + 0.0301 NIR \quad (2.17)$$

The weighted sums developed by Horne (2003) for IKONOS channels:

$$TCT_{IKONOS-bands1} = 0.326 BLU + 0.509 GREEN + 0.560 RED + 0.567 NIR \quad (2.18)$$

$$TCT_{IKONOS-band2} = -0.311 BLU - 0.356 GREEN - 0.325 RED + 0.819 NIR \quad (2.19)$$

$$TCT_{IKONOS-band3} = -0.612 BLU - 0.312 GREEN + 0.722 RED - 0.081 NIR \quad (2.20)$$

$$TCT_{IKONOS-band4} = -0.650 BLU + 0.719 GREEN - 0.243 RED - 0.031 NIR \quad (2.21)$$

TCT has been adopted in archaeology by several authors, see, for example Campana 2003; Lasaponara and Masini 2007b; Traviglia 2008.

Figure 2.10a shows a composition (RGB) of the first three TCT components computed from Landsat ETM 7 (2000) related to the drainage basin of the river Rio Grande (Southern Peru). Figure 2.10b depicts a subset of Fig. 2.10a focusing the famous Nasca lines. The colours enable us to discriminate the desert area in red (brightness), the vegetation cover mainly in the fluvial oases in green and, finally, the area with higher moisture content in blue and/or light blue (wetness).

2.3.4.2 Principal Component Analysis (PCA)

In order to identify the small spectral signals linked to archaeological features, some authors (see for example Zhang et al. 2010; Deroin et al. 2011; Lasaponara et al. 2011; Traviglia and Cottica 2011) adopted Principal Component Analysis (PCA).

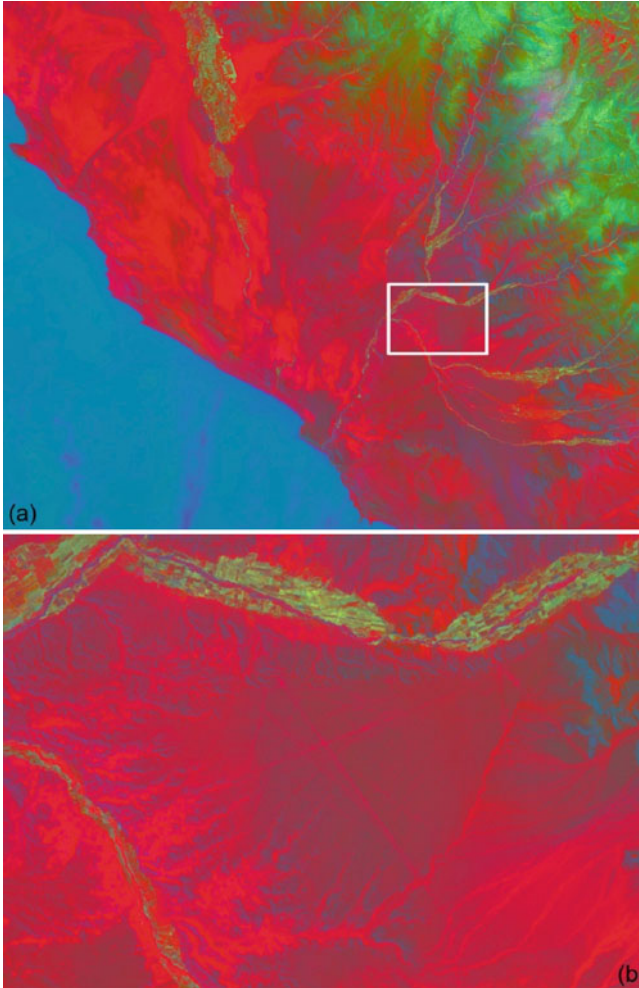


Fig. 2.10 RGB composition of the first three TCT components (brightness, greenness and wetness) computed from Landsat ETM 7 (2000). (a) Drainage basin of the river Rio Grande (Southern Peru); (b) subset including the Nasca lines. The colours enable us to discriminate the desert area in *red* (brightness), the vegetation cover mainly in the fluvial oases in *green* and the area with higher moisture content in *blue* and/or *light blue* (wetness)

It is a linear transformation which decorrelates multivariate data by translating and/ or rotating the axes of the original feature space, so that the data can be represented without correlation in a new component space (see Fig. 2.11). In order to do this, It is first computed: (i) the covariance matrix (S) among all input spectra bands (each element of S is calculated by using formula 2.22), then (ii) eigenvalues and eigenvectors of S in order to obtain the new feature components.

Principal Component Analysis

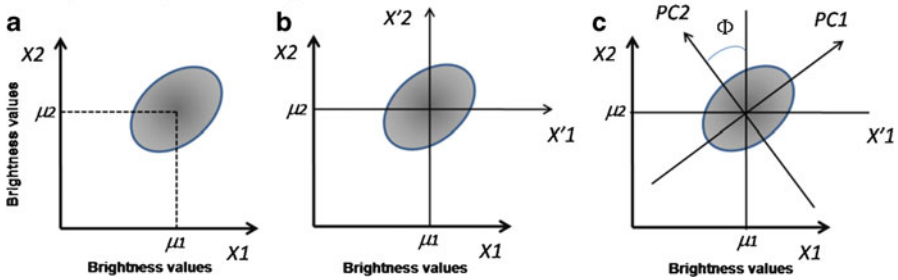


Fig. 2.11 PCA decorrelates multivariate data by translating and/or rotating the axes of the original feature space. The data can be represented in a new component space without correlation

$$\text{cov}_{k_1 k_2} = \frac{1}{n \times m} \sum_{i=1}^n \sum_{j=1}^m (SB_{i,j,k_1} - \mu_{k_1}) \times (SB_{i,j,k_2} - \mu_{k_2}) \quad (2.22)$$

where k_1, k_2 are two input spectral channels, $SB_{i,j}$ is the spectral value of the given channel in row i and column j , n number of row, m number of columns, μ is the mean of all pixel $SB_{i,j}$ values in the subscripted input channels.

The percent of total dataset variance explained by each component is obtained by formula 2.23:

$$\% i = 100 \times \vartheta_i / \sum_{i=1}^k \lambda_i \quad (2.23)$$

where λ_i are eigenvalues of S

Finally, a series of new image layers (called eigenchannels or components) are computed (using formula 2.24) by multiplying, for each pixel, the eigenvector of S for the original value of a given pixel in the input bands

$$P_i = \sum_{k=1}^n P_k \times u_{k,i} \quad (2.24)$$

where P_i indicates a spectral channel in component i , $u_{k,i}$ eigenvector element for component i in input band k , P_k spectral value for channel k , number of input band.

A loading, or correlation R , of each component i with each input band k can be calculated by using formula 2.25.

$$R_{k,i} = u_{k,i} \times (\lambda_i)^{1/2} \times (\text{var}_k)^{1/2} \quad (2.25)$$

where var_k is the variance of input data k (obtained by reading the k th diagonal of the covariance matrix)

The PCA transforms the input multispectral bands in new components that should be able to make the identification of distinct features and surface types

easier. This is a direct result of two facts: (i) the high correlation existing among channels for areas that do not change significantly over the space; and (ii) the expected low correlation associated with higher presence of noise.

The major portion of the variance in a multi-spectral data set is associated with homogeneous areas, whereas localised surface anomalies will be enhanced in later components. In particular, each successive component contains less of the total dataset variance. In other words, the first component contains the major portion of the variance, whereas, later components contain a very low proportion of the total dataset variance. Thus they may represent information variance for a small area or essentially noise and, in this case, it must be disregarded. Some problems can arise from the fact that eigenvectors cannot have general and universal meaning since they are extracted from the series (Fig. 2.12).

The main difference between TCT and PCA is that the latter computes the weight coefficients from the data and this is the reason why the meaning of the PCA components is dataset dependent. TCT has for each component a specific physical meaning because the transformation is based on weight coefficients which are empirically obtained for each sensor and surface types and characteristics.

2.3.4.3 IHS Transform

The RGB color space represents the amount of red, green and blue components in a color, and therefore it is not easy to distinguish one colour from another only using the RGB colour coordinates. To overcome this limitation, some authors suggest the use of IHS transform which converts three images from the RGB space into the Intensity, Hue and Saturation (IHS) color space. The IHS space provides parameters and information closer to the human colour perception, in particular:

- (i) Intensity is the overall brightness and informs us about how close the image is to black or white.
- (ii) Hue provides information about the actual perceived color (i.e. the dominant or average wavelength of light)
- (iii) Saturation informs us about the purity of the color

Similarly to TCT and PCA, IHS performs a rotation from the RGB axis to a new orthogonal IHS. This axis rotation can be obtained by using different formulas which enable us to separate spatial (I) and spectral (H, S) information from a standard RGB image. Among the number of diverse combinations to obtain the new space, herein we report the Pellemans' equations (Pellemans et al. 1993) in formula 2.26.

$$\begin{bmatrix} x \\ y \\ z \end{bmatrix} = \begin{bmatrix} \frac{1}{\sqrt{3}} & \frac{2}{\sqrt{3}} & 0 \\ -\frac{2}{\sqrt{3}} & \frac{1}{\sqrt{3}} & 0 \\ 0 & 0 & 1 \end{bmatrix} \begin{bmatrix} \frac{1}{2} & 0 & \frac{1}{\sqrt{2}} \\ 0 & 1 & 0 \\ -\frac{1}{\sqrt{2}} & 0 & \frac{1}{\sqrt{2}} \end{bmatrix} \begin{bmatrix} B \\ G \\ R \end{bmatrix} \quad (2.26)$$

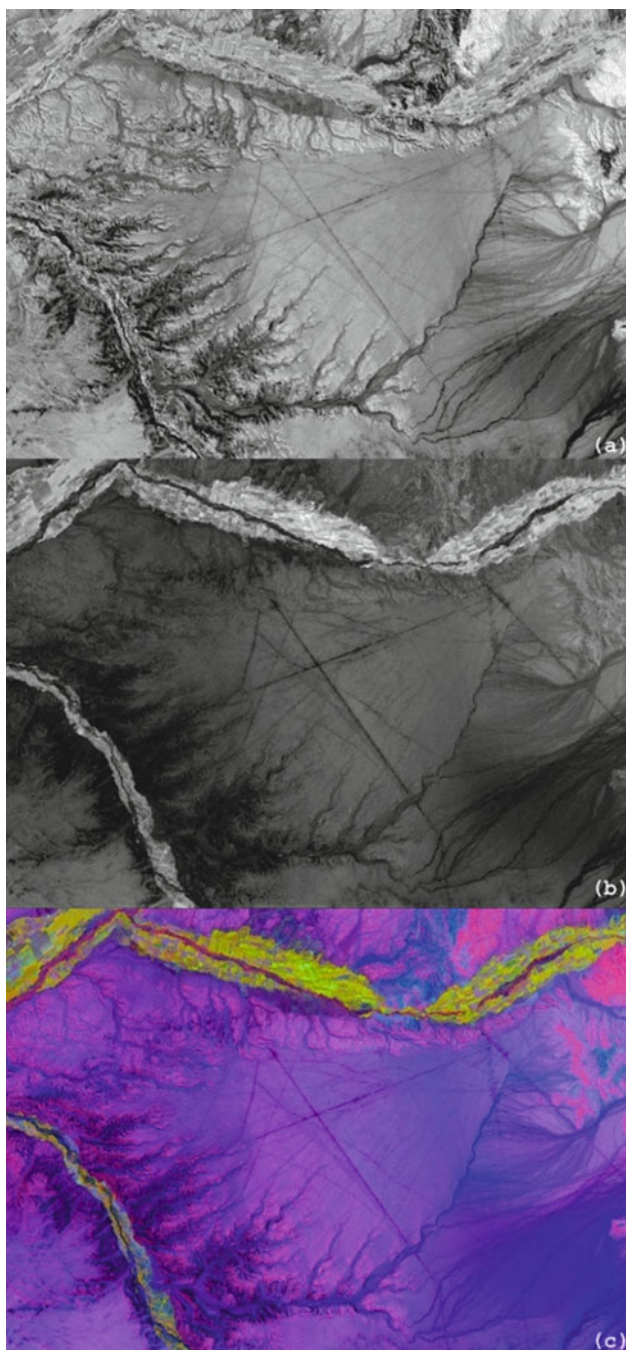


Fig. 2.12 Results from PCA obtained for an area at South of Rio Ingenio characterized by the presence of Nasca Lines. PCA is computed using Landsat ETM 7 (2000). (a) PC2; (b) PC3; (c) RGB composition (R = PC2, G = PC3, B = PC4). PC2 and RGB emphasize the geoglyphs, PC3 puts in evidence the vegetation in the fluvial oasis

The value of H, S and I can then be computed as:

$$H = \tan^{-1} \left(-\frac{\sqrt{z}}{\sqrt{x}} \right) \quad (2.27)$$

$$S = \cos^{-1} \left(\frac{\frac{\sqrt{y}}{\sqrt{x+y+z}}}{\Phi_m(H)} \right) \quad (2.28)$$

$$I = \frac{(x + y + z)}{I_M(H, S)} \quad (2.29)$$

Where $\Phi_m(H)$ is the maximum colatitude for a given hue, $I_M(H, S)$ is the maximum intensity for a given hue and colatitude.

The transformation from the RGB color space to a given IHS space is characterized by the following properties: (i) nonlinearity (ii) reversibility and (iii) independent of each component from the others i.e. it may be varied without affecting the others.

Thanks to these properties, IHS is considered an ideal tool for image processing ranging from contrast enhancement to image fusion aimed at (i) enhancing the spatial content and (ii) preserving the spectral properties of the data set to be processed.

This transformation has been used in archaeology, see for example Campana (2003) and Aminzadeh and Samani (2006).

2.4 Spatial Enhancement

2.4.1 Image Enhancement in the Spatial Domain

The spatial domain refers to pixel aggregation which composes an image that may be manipulated according to the “investigation needs”. Within this domain, pixels are the “*spatial variables*” being that they are a function (Treitz and Howarth 2000) of spatial position. Therefore, pixel values and position inform us about the spatial detail namely providing the information content of the scene. Image enhancement in the spatial domain operates directly (i) on the given pixels, which are the basic building block of a remotely sensed image and also on (ii) the neighbouring areas, which provide the spatial arrangement of information. As an example, features linked to buried remains may refer to a roman villa if they are displaced with a rectangular shape, or to Neolithic settlement in the case of circular arrangement, etc.

To extract information content from a digital image, we can use spatial analyses to capture features, patterns and trends using distance and spatial relationships, in particular: (i) measuring the interdependence of brightness values, (ii) quantifying

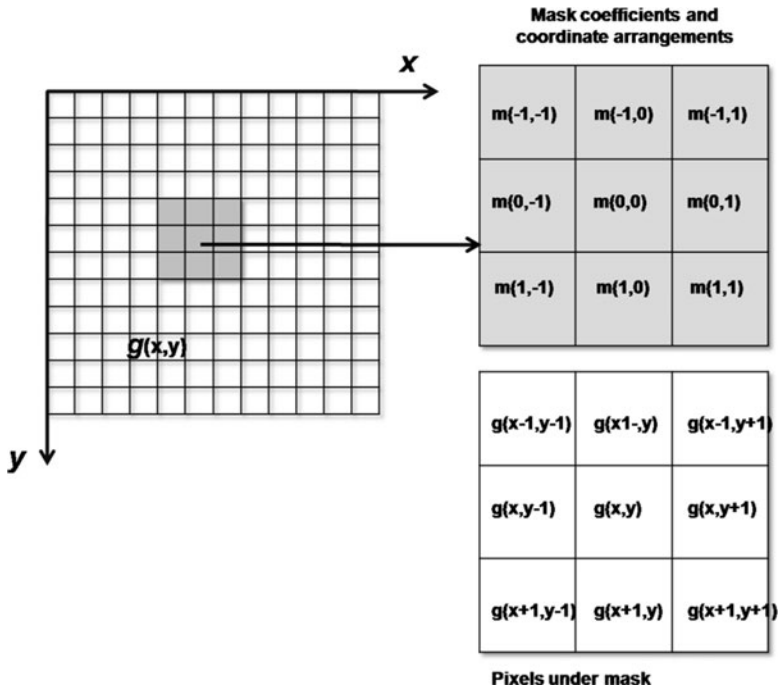


Fig. 2.13 Grey indicates a (moving) mask, also known as kernel, used to assign given weights to the pixels under mask in order to carry out local mathematical computation to obtain a new output image

spatial distribution and (iii) describing spatial clustering or random distribution of features.

Spatial enhancement highlights geometric detail in a digital scene linked to changes in brightness values which are generally influenced by the surrounding pixels. The use of filtering determines variations in the geometric detail at both local (contextual) and global (whole image) level in the perception of the information content. Figure 2.13 shows the spatial analysis which is generally conducted using a (moving) mask also known as kernel to assign given weights to the pixels under mask.

The spatial filtering process may enhance or smooth these image characteristics to extract or leave out pattern features from the background. The spatial filtering process is based on a 'local' mathematical operation generally applied using a two dimensional moving window ('kernel') to obtain a new output image from the results of the given mathematical operation (kernel, averaging process or whatever).

The spatial information content is also evident in the frequency domain and, therefore, it may be also captured in this domain.

For a given scene (or a subset), spatial frequency is defined as the number of changes in brightness value per unit distance. Therefore, few changes in brightness

value corresponds to low-frequency detail, whereas, dramatic changes over short distances are referred to as a high-frequency detail.

Low frequency image characteristics refer to areas quite homogeneous with relatively little changes in pixel brightness values over a large region. High frequency image characteristics refer to heterogeneous areas with dramatic changes over a very short distance. This is when abrupt changes are present, as for example for scan line errors or fragmented landscapes, defined as ‘roughness’ by Lillesand and Kiefer (2000).

Generally within an image we may find high, medium and low frequencies which can be emphasized or suppressed according to the information of interest and/or the object, shape, pattern we need to hide or unveil.

The spatial properties of a digital image can be promptly improved according to the *investigation needs* using a variety of different processing techniques, such as:

- (i) Fourier analysis and wavelet;
- (ii) Fractal analysis power law transformation;
- (iii) spatial filtering;
- (iv) geospatial analysis.

2.4.2 *Fourier Transformation*

Detailed analysis on the frequency content of an image can be attained by using the Fourier transform which involves the transformation of the original coordinate space into a new two dimension space spectrum. Image enhancement or smoothing may be arranged by suppressing low or high spatial frequencies. Low, medium and high frequency components are first identified through the direct Fourier transform (formula 2.30), then removed, according to the data processing aims. Finally, a new image is generated using the inverse Fourier transform, which is expressed in formula 2.31:

$$F(x, y) = \sum_{u=0}^{N-1} \sum_{v=0}^{N-1} f(u, v) e^{j2\pi(xu+yv)/N} \quad (2.30)$$

In formula 2.30 $f(u,v)$ is the image in the spatial domain, N is raw and line pixel number, the exponential expresses the basis functions of Fourier transformation as sine and cosine waves with increasing frequencies, finally $F(x,y)$ is the $f(u,v)$ in the Fourier transformation.

As an example, $F(0,0)$ represents the component of the image which corresponds to the average brightness and $F(N-1,N-1)$ is the highest frequency. The Fourier image can be re-transformed to the spatial domain, by using Eq. 2.31:

$$f(u, v) = \frac{1}{N^2} \sum_{x=0}^{N-1} \sum_{y=0}^{N-1} F(x, y) e^{-i2\pi\left(\frac{xu}{N} + \frac{yv}{N}\right)} \quad (2.31)$$

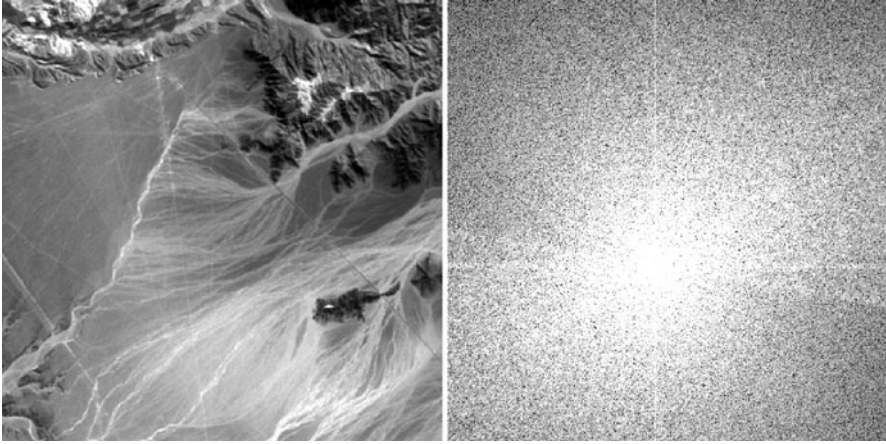


Fig. 2.14 Fourier transform (magnitude or real part) for ASTER image of Nasca Lines

where the $\frac{1}{N^2}$ is a normalization term in the inverse transformation. It can be applied to the forward transform instead of the inverse transform, but it should not be used for both of them.

The results of the Fourier Transform are complex numbers which are displayed using two images for the *real* and *imaginary* part, respectively or, equivalently, with *magnitude* and *phase*.

The Fourier Transform enables us to access the geometric characteristics of a spatial domain image, being easy to identify and process given frequencies of the image, so modifying the geometric structure in the spatial domain. In image processing, the Fourier image is often shifted in order to display $F(0,0)$ (i.e. the image mean) in the center of the image and the higher frequency components further away from the center. Moreover, being that the dynamic range of the Fourier coefficients is too large, a logarithmic transformation is generally applied to display it on the screen. Figure 2.14 shows an example of Fourier transform.

This type of analysis and processing may be very useful for noise removal and image restoration, low, high frequency filtering, edge detection, radiometric correction, and image to image registration. In particular, noise is easier identified in frequency domain than in spatial domain. This is the main reason for the increasing use of Fourier in the pre-processing data analysis. As an example, ASTER SWIR imagery present a radiometric error caused by deterioration of the scanning system (known as ‘six-line banding’). This data set cannot be employed without a destriping method which can be easily performed using Fourier. This type of noise is clearly visible in the spectrum as features at 90° to their direction in the spatial domain of the original scene.

One more example can be the presence in the spatial domain of stationary periodic noise, which produces, in the frequency domain, a single-frequency

sinusoidal function appearing as bright points. A line connecting the points is always perpendicular to the orientation of the noise lines in the original image.

Nevertheless, significant limitations in the use of Fourier analysis are: (i) the fact that it works globally and (ii) it is not possible to identify direct relationship between a specific components and frequencies.

2.4.3 Wavelet Transform

Recently, wavelet-based data analysis has become one of the fastest growing research areas, being used for a number of different fields and applications. Wavelets are mathematical functions which were developed independently in diverse application fields ranging from mathematics, electrical engineering, quantum physics, and seismic geology. In the last years, wavelet has rapidly covered new application fields, spanning from communication systems to imaging including satellite data analysis.

Signal wavelet decomposition using Discrete Wavelet Transform (DWT) provides an alternative to the Discrete Fourier Transform (DFT). Wavelet transform offers a number of advantages compared to traditional Fourier methods especially in searching for discontinuities and sharp spikes in analyzing signal. The main ability of DWT, which is also the benefit of DWT over DFT, is its multi-resolution time-scale analysis. Moreover, wavelet transform can be used to analyze signals which contain non-stationary power at many different frequencies (Daubechies 1990).

Given a discrete a discrete sequence x_m , the continuous wavelet transform is defined as the convolution of x_m with a scaled and translated version of the function $F_{0n}(\varepsilon)$, which is called mother wavelet, as in formula 2.32:

$$W_n(s) = \sum_{m=0}^{N-1} x_m F^* \left[\frac{(m-n)\delta t}{s} \right] \quad (2.32)$$

where F^* indicates the complex conjugate.

It is really important to note that variations in the transformed signal is function of two variables, n and s , the translation and scale parameters, respectively. Through the variations of wavelet scale (s and n), it is possible to obtain information about the amplitude of any features versus the scale and how this amplitude varies with time/space. The function F is the wavelet Function. To be “admissible” as a wavelet, F must have zero mean and be localized in both time (space, in the case of image processing) and frequency domain (Farge 1992).

One criticism of wavelet analysis is the arbitrary choice of the mother wavelet function, which is obviously linked with the data analysis purposes.

Figure 2.15 shows an example of the wavelet transform applied to the same image as in Fig. 2.14.



Fig. 2.15 Wavelet transform performed by using open source software IRIS for the same image as in Fig. 2.14

The shape of the wavelet function should reflect the type of features present in signal/image under processing. As an example, for abrupt changes, such as sharp jumps or steps, the Harr function is the most recommended, whereas in the case of smooth variations a damped cosine function is more adequate.

Wavelet function may be complex or real. In the first case it provides information relating to both amplitude and phase, whereas a real wavelet only provides a single component which is very useful to identify and to isolate peaks or discontinuities.

Wavelets split the data into different frequency components, and then study each component with a resolution matched to its scale. In the field of image processing, DWT acts in this way: an image is decomposed, with each level corresponding to a coarser resolution band.

There are two basic types of wavelet transforms: (i) one, widely used for image compression and cleaning (noise and blur reduction), designed to be easily reversible (invertible); (ii) the second type of wavelet transform is designed for signal analysis; for example, to detect noise, to study signals, to determine how the frequency content of a signal evolves.

Some techniques only focus on the image enhancement without any reduction of noise, such as the method proposed by Fu (Wang et al. 2010) based on the histogram equalization in wavelet domain; whereas others mainly focus on the noise reduction. Many algorithms consider both detail enhancement and noise reduction, as in the case of Pengxin Zeng (Zeng et al. 2004), who proposed an algorithm which offers a good compromise between noise reduction and subtle detail enhancement.

Wavelet transformations are also used in field of cultural heritage mainly in the processing of georadar and geomagnetic data (Bloisi et al. 2010). Another application is the data fusion between panchromatic image and multispectral data or between satellite radar and multispectral images (see Chap. 4 and references therein quoted).

2.4.4 Fractal Analysis

Fractal concept is quite close to self-similarity which means that a small part of a given object/image/pattern exhibits the same statistical properties as the whole, and, therefore, it appears as “scale invariant”. In other words, it is the same (in terms of mathematical properties) at all scales of observation. The self-similar elements are also related in scale by a non-integral power-law. Self-similar objects with parameters N and S are described by a power law such as

$$N = s^d \quad (2.33)$$

where $d = \frac{\ln N}{\ln s}$ is the “dimension” of the scaling law, known as the Hausdorff dimension.

Fractals are a particularly interesting class of self-similar objects. It is important to highlight that a pattern is self-similar if it is made up of smaller-scale copies of itself, but this is not enough to be fractal, which requires "fractional dimension". In other words the fractal dimension d must be a fraction, not an integer.

Numerous studies have been performed to analyze the fractal characteristics of modern human settlement mainly focusing on boundaries for both large and small urban areas (see for example Telesca et al. 2009 and references therein quoted).

Within archaeological sites, Brown and Witschey (2003) investigated the fractal characteristics of Maya settlement considered fractal at both intra-site and inter site levels. At the intrasite level Brown's analysis pointed out that "buildings form a pattern of repeated, complex, nested clusters of clusters". At the intersite organization they found that "(1) the size–frequency distribution of settlements is fractal; (2) the rank–size relation among sites is fractal; and (3) the geographical clustering of sites is fractal." The main point suggested by Brown was the consideration that the fractal model may explain the cycle of rising, flourishing and collapse of early South American states. They were self-organized critical systems therefore, quite far from equilibrium and this may explain why some of them were highly susceptible to major changes in the face of minor forces.

Brown and Witschey (2003) also provided examples of other cultural settlements where this model and distribution is untenable, because not supported by empirical data. For example, the orthogonal grid pattern of a Roman city tends to be Euclidean rather than fractal, although its fractality depends on the details of the grid squares. Brown and Witschey (2003) mainly focused on the empirical verification of the fractal behavior and also in the establishing relationships between the Pareto exponents and social, economic, geographic processes and geometric distribution of archaeological settlement. In order to assess if the ancient settlement distribution exhibits a fractal geometry, the spatial organization of the buildings must be logically and geometrically self-similar and mathematically of fractional dimension, namely it must also be related in scale by a non-integral power-law.

Over the years, numerous techniques for fractal dimension computation have been developed and also applied to digital image domain. Fractal dimension can be applied to image data analysis for estimating various parameters, such as, roughness, texture, segmentation, surface roughness, shape irregularity, etc.

Any kind of set, such as points, lines, surfaces, multi-dimensional data, or time series may be fractal. For a regular 2-dimensional curve the fractal dimension is 1. Spatial fractal curves are characterized by fractal dimension larger than 2. The fractal dimension can be computed using a variety of different methodologies, herein we focus on the box-counting method which is one of the most widely used approaches.

The box-counting method computes the degree of irregularity of borders; therefore higher the fractal dimension, more irregular the border. The image of the settlements under investigation must be divided in non-overlapping cells of size L . Then the number of cells occupied by at least one point belonging to the border is

computed. The procedure is iterated for different sizes L and the number of cells as a function of the size L behaves as a power-law for fractal borders:

$$N(L) \approx L^{-df_{\text{BOX}}} \quad (2.34)$$

where df_{BOX} is the box-counting fractal dimension:

$$df_{\text{box}} = \lim_{L \rightarrow 0} \frac{\ln(N(L))}{\ln(1/L)} \quad (2.35)$$

$$df_{\text{BOX}} = \lim_{L \rightarrow 0} \frac{\ln(N(L))}{\ln\left(\frac{1}{L}\right)} \quad (2.36)$$

The estimate of the fractal dimension is performed calculating the slope of the line fitting the Eq. 2.1 in its linear part.

2.4.5 Spatial Filtering

All the previous techniques, including Fourier, Wavelet, and Fractal analysis may be time consuming and may also require an intense user-interaction. There are a number of other techniques for feature enhancement and extraction which are more user- friendly and also implemented in a number of commercial software (such ENVI, ERDAS, PCI) and also in open source programs, such as GRASS, IRIS, etc.

Spatial filtering can be used to highlight or subdue edges, features and spatial relationships among neighboring pixels. High pass filters enhance differences, whereas low pass filters smooth them.

Spatial domain process can be described as

$$g(x, y) = T[f(x, y)] \quad (2.37)$$

where $g(x,y)$ is the output image, T is an operator, $f(x, y)$ is the input image.

The spatial filtering generally involves some types of convolution techniques that evaluate pixels on the basis of the spectral values of its neighboring. As we are only concerned with digital images, we will restrict the discussion to the discrete convolution into two dimensions (see Eq. 2.38). where the sum is taken over all values of x and h for which non zero results exists

$$y(m, n) = \sum_{i=-k}^k \sum_{j=-k}^k x(m + i, n + j)h(i, j) \quad (2.38)$$

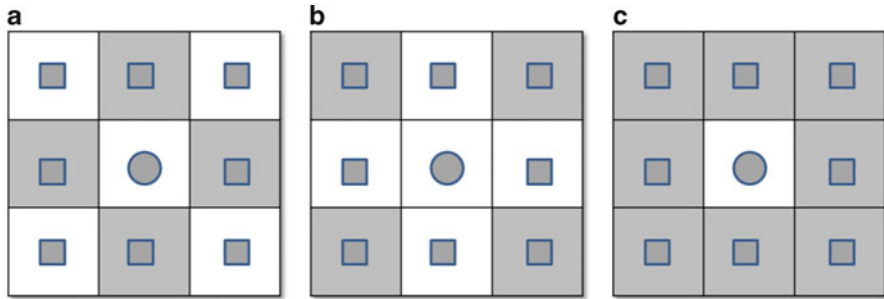


Fig. 2.16 (a) Tower contiguity, (b) bishop contiguity, (c) queen contiguity

It is really important to highlight that the convolution corresponds to the application of a template (or kernel matrix), which can be directly found in the image processing software, such as ENVI, PCI, ERDAS (1999) or can also be promptly customized according to specific computation needs. In the following sub-sections the most common filtering techniques are briefly presented and discussed along with the most common corresponding templates which can be also varied to improve the data processing.

All the image processing software programs offer the possibility to use pre-defined kernels but it is also possible to customize shape, size and weight values of the kernel. The pre-defined kernel matrix has specific dimensions generally there are odd-number sized kernels starting from 3×3 upwards to larger window size. Different shapes may be used, for example directional or contiguity kernel matrix. Figure 2.16 shows some possible kernel different from the existing methods which take their name from the game of chess. They are called tower contiguity (Fig. 2.16a), bishop contiguity (Fig. 2.16b) and queen contiguity (Fig. 2.16c).

2.4.5.1 Low Pass Filters

Low pass filters are also known as smoothing filters because they act to remove high spatial frequency details and preserves the low frequency components. In its simplest formulation the pass filter contains the same weights in each kernel element, replacing the center pixel value with an average of the surrounding values. Figure 2.17 describes the nature of the mathematical operation of this moving kernel matrix.

Low pass filters are employed to emphasize the broader changes present within the image scene, but is very useful for noise removal or reduction and as an intermediate step of data processing oriented to image enhancement.

Fig. 2.17 The low pass filter kernel

1/9	1/9	1/9
1/9	1/9	1/9
1/9	1/9	1/9

Fig. 2.18 The high pass filter kernel

-1	-1	-1
-1	8	-1
-1	-1	-1

2.4.5.2 High Pass Filters

High pass filters act to remove low spatial frequency details and preserve the high frequency components linked to local variations. This operation can be obtained by subtracting the results of the low pass filter from the original image so obtaining a new image with enhanced local contrast (Richards and Jia 2006). This method has been used as the simplest way to obtain high spatial frequency image. Figure 2.18 describes the nature of the mathematical operation of this moving kernel matrix characterized by a high central value, typically surrounded by negative weights.

High pass filters can only have odd kernel dimensions. They are used for image sharpening or edge enhance.

The high pass filter enhances spatial frequencies that are less than the size of the kernel matrix used in the operation. Therefore the selection of kernel size produces a strong control on the level of detail generated from the process. For instance, very small anomalies (archaeological remains, or linear pattern anomalies) require small kernels size; whereas very large features, such as building, geological faults, etc. require much larger kernels in order to effectively enhance their properties within the imagery.

2.4.5.3 Median Filters

Median filter replaces each center pixel with the median value (not the average) within the neighborhood specified by the Kernel size. The median filter search for the “middle” value (i.e. median pixel value) in a given set of data. Therefore, it acts as a smoothing in an image while preserving edges larger than the kernel dimensions. Weighted Median Filter (more general Median filter) may be defined ad hoc to remove or retain a predefine set of features

$$CT_{filtered} = \frac{\sum \{[ABS(CT - a) + \dots + ABS(CT - a8)]\}}{8} \quad (2.39)$$

Where:

a1, . . . ,a8 are grey pixel values into the template

CT is the grey value for pixel at the center of the template

2.4.5.4 Gaussian Filters

A Gaussian filter is a smoothing operator quite similar to the mean filter, but based on a different kernel (with Gaussian shape), which smooths preserving edges more than a mean filter with a similar size.

The Gaussian convolution function must be applied to an odd dimension kernel. In the image processing, the Gaussian distribution is a 2-D function formalized as in formula:

$$G(x, y) = \frac{1}{2\pi\sigma^2} e^{-\frac{x^2+y^2}{2\sigma^2}} \quad (2.40)$$

It is assumed that the distribution has a zero mean.

Actually, it is possible to use the Gaussian operator for both smoothing and enhancement purposes even using a corresponding template. The standard deviation of the Gaussian determines the degree of smoothing and, for example Fig. 2.19 shows the equivalent convolution kernel that approximates a Gaussian low pass filter.

Fig. 2.19 Discrete approximation to Gaussian function

0.0007	0.0256	0.0007
0.0256	0.8948	0.0256
0.0007	0.0256	0.0007

2.4.5.5 Derivative Edge Detection Methods

For a given image, the pixel value, such as brightness, or temperature, or vegetation indices, can be expressed as a discrete function ϕ of coordinates x and y . For this function we can compute the first, the second derivative and the vector gradient according to formulas 2.41, 2.42, 2.43, 2.44

$$\nabla\Phi(x, y) = \frac{\partial}{\partial x} \phi(x, y)\hat{i} + \frac{\partial}{\partial y} \phi(x, y)\hat{j} \quad (2.41)$$

$$\nabla^2\Phi(x, y) = \left[\frac{\partial^2}{\partial x^2} \Phi(x, y)\hat{I} \right] + \left[\frac{\partial^2}{\partial y^2} \Phi(x, y)\hat{J} \right] \quad (2.42)$$

$$\alpha(x, y) = \tan^{-1} \frac{\nabla_2}{\nabla_1} \quad (2.43)$$

$$|\nabla| = \sqrt{\nabla_1^2 + \nabla_2^2} = \sqrt{\left[\frac{\partial}{\partial x} \phi(x, y) \right]^2 + \left[\frac{\partial}{\partial y} \phi(x, y) \right]^2} \quad (2.44)$$

where \hat{i}, \hat{j} are a pair of unit vectors.

A digital image defines a discrete space therefore its derivative and gradient can be easily expressed as differences.

A number of filters are obtained using the first derivative or the second derivative and considering the spatial variations in all the possible directions or in specific directions, as in the so called directional filters which selectively enhances image features having specific direction components (gradients).

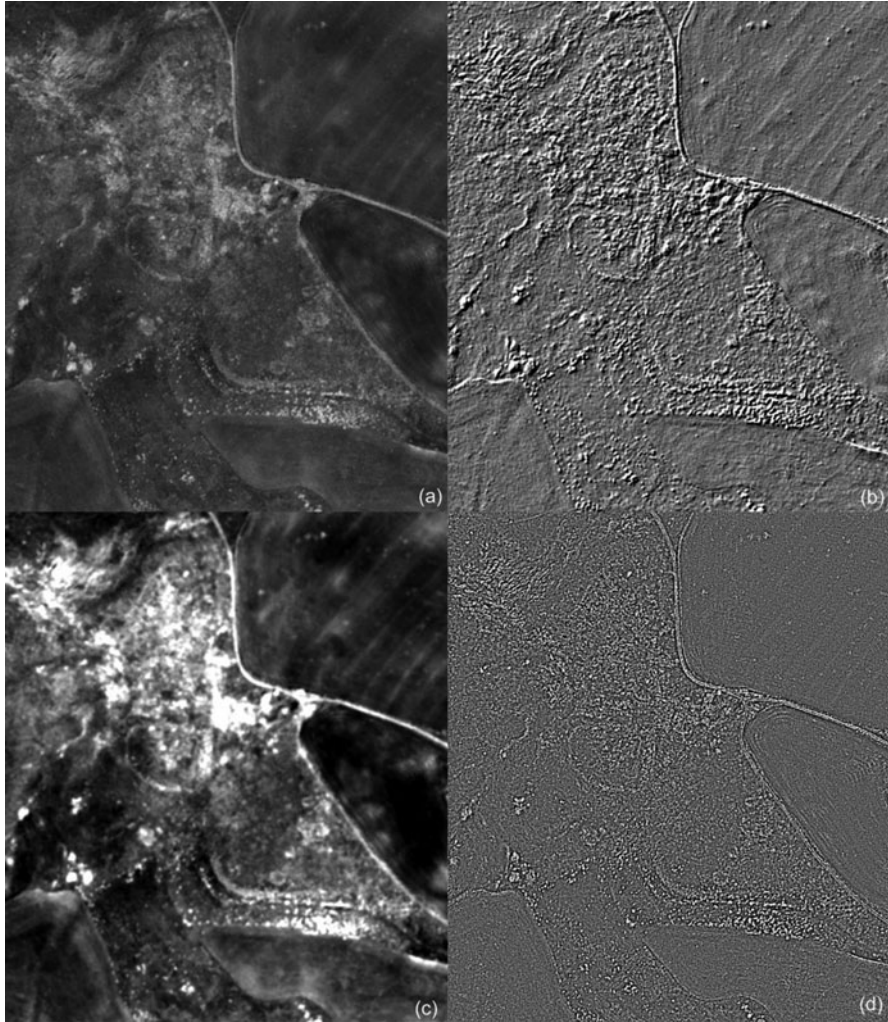


Fig. 2.20 Results of spatial filters on a panchromatic image (a) related to the medieval village of Irsi (Southern Italy): (b) directional filter, (c) Gaussian low pass, (d) High pass filter

As an example, one of the most used filter is the Laplacian filter based on a second derivative edge enhancement which operates without regard to edge direction.

Finally, directional filters have been specifically devised to detect edges running in given direction such as: (i) vertically and horizontally relative to the pixel grid, or (ii) at a given angle relative to the pixel grid.

Edge detection has become one of the fastest growing research areas, being used for a number of different fields and applications, among the others we only cite as examples signal imaging, biomedical data analysis, face recognition and satellite image processing including Archaeology, as shown in Fig. 2.20.

2.4.5.6 Mathematical Morphological Filtering

Mathematical morphology is a non-linear image processing method, which is based on the use of two-dimensional convolution operation and includes a big number of different operators, spanning from the simplest erosion, dilation, opening operation and closing, which are the basis operations of mathematical, to the more complex, such as geodetic transformations or hit-and-miss transformations (see, for example Soille 2003).

Mathematical morphology enables the analysis of the spatial relationships between groups of pixels, thus providing a complementary strategy to the analysis of the spectral signature of single pixels. Starting from the mid-1980s (see for example Haralick et al. 1987) successful applications of MM have been reported in geoscience and remote sensing for noise reduction, edge detection, feature extraction and classification. Nevertheless, recent advances in the theory of mathematical morphology are still largely unexplored.

2.5 Remote Sensing and Geospatial Data Analysis

Geospatial data analysis includes a set of geostatistic tools useful for the characterization of spatial variation, prediction, simulation and autocorrelation. Applications of geostatistics are found in a wide range of fields including biology, environmental science, geography, geology, data mining and remote sensing.

In the field of remote sensing variogram analysis (also known as semivariogram) has been the most widely used geostatistic tool applied to describe the correlation between image pixels in close proximity to each other. Variance is obviously related to the size of objects and spatial resolution. It is considered a powerful tool to describe the spatial dependency of data using measures of local variance namely the frequency of changes within the image scene.

Geospatial data analysis in archaeology has been approached by some researchers (Burke et al. 2008; Meghan and Howey 2011), but up to now only few examples deal with the application of geostatistics to image processing for archaeological investigations (Lasaponara and Masini 2010).

2.5.1 *The Spatial Autocorrelation: Basic Concepts*

Spatial autocorrelations take into account the spatial attributes of geographical objects under investigation, evaluate and describe their relationship and spatial patterns also including the possibility to infer such patterns at different times for the study area. The spatial patterns are defined by the arrangement of individual entities in space and the spatial relationships among them. Spatial autocorrelations in the field of archaeological investigations measure the extent to which the occurrence of one object/feature/site is influenced by similar objects/features/sites in the adjacent areas.

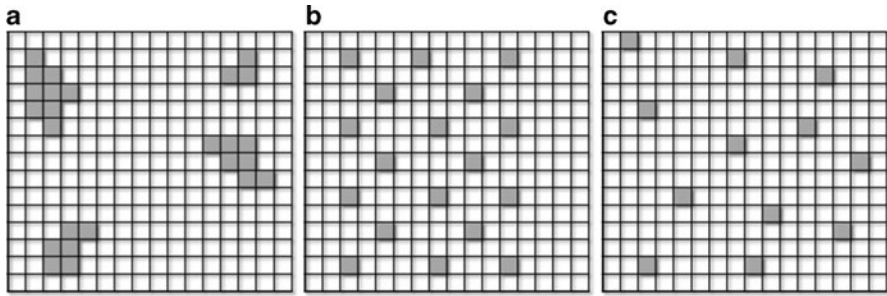


Fig. 2.21 Possible spatial distributions (a) positive spatial autocorrelation, (b) negative spatial autocorrelation, (c) null autocorrelation

As such, statistics of spatial autocorrelation provide (i) indicators of spatial patterns and (ii) key information for understanding the spatial processes underlying the distribution of object/feature/site and/or a given phenomenon under observation.

Geographical observations should be arranged in spatial and temporal order, by latitude and longitude, and historical periods. In this context time series data, such aerial and satellite images can provide useful traces of past human activities and, therefore, can enable us: (i) to some extent predict the amount and types of interaction, (ii) to investigate spatial predictions between objects/features/sites and also to infer potential relations considering different “historical” time windows being that “Everything is related to everything else, but nearest things are more related than distant things” (Tobler 1990).

In absence of spatial autocorrelation the complete spatial randomness hypothesis is valid: the probability to have an event in one point with defined (x, y) coordinates is independent of the probability to have another event belonging to the same variable. The presence of spatial autocorrelation modifies that probability; fixed a neighbourhood for each event, it is possible to understand how much it is modified from the presence of other elements inside that neighbourhood.

A distribution can show three types of spatial autocorrelation: (i) the variable exhibits positive spatial autocorrelation (Fig. 2.21a) when events are near and similar (clustered distribution); (ii) the variable exhibits negative spatial autocorrelation (Fig. 2.21b) when, even if events are near, they are not similar (uniform distribution); the variable exhibits null autocorrelation (Fig. 2.21c) when there are no spatial effects, neither about the position of events, or their properties (random distribution).

2.5.2 The Spatial Autocorrelation: Basic Formulations

The presence of autocorrelation in a spatial distribution is caused by two effects, that could be clearly defined (Gatrell et al. 1996), but not separately studied in the practice: (i) first order; and (ii) second order effect.

- (i) First order effects depend on the region of study properties and measure how the expected value (mean of the quantitative value associated to each spatial event) varies in the space with the following expression:

$$\hat{\lambda}_\tau(s) = \lim_{ds \rightarrow 0} \left\{ \frac{E(Y(ds))}{ds} \right\} \quad (2.45)$$

where ds is the neighbourhood around s , E is the expected mean and $Y(ds)$ is the events number in the neighbourhood.

- (ii) Second order effects express local interactions between events in a fixed neighbourhood, that tends to the distance between events i and j . These effects are measured with covariance variations expressed by the limit:

$$\gamma(s_i, s_j) = \lim_{ds_i, ds_j \rightarrow 0} \left\{ \frac{E(Y(ds_i)Y(ds_j))}{ds_i ds_j} \right\} \quad (2.46)$$

where symbols are similar to those used in Eq. 2.1.

The characterization of spatial autocorrelation requires detailed knowledge on (i) quantitative nature, (ii) geometric nature of the data set under investigation; in detail:

- (i) quantitative nature, also called intensity of the spatial process, provides information on space occurrence of a given variable (Murgante et al. 2008), to understand if events are similar or dissimilar.
- (ii) geometric nature needs the conceptualization of geometric relationships, usually done using the following matrixes:
- (a) a contiguity matrix to assess if events influence each other;
 - (b) a distance matrix to consider at which distance the events influence each other (distance band);
 - (c) a matrix of spatial weights to estimate how strong this influence is.

Concerning the distance matrix, a method should be established to calculate distances in module and direction. The Euclidean distance (3), is the most used.

$$d_E(s_i, s_j) = \sqrt{(x_i - x_j)^2 + (y_i - y_j)^2} \quad (2.47)$$

As for any type of dataset also in the case of digital image analysis there are many indicators of spatial autocorrelation, that can be distinguished into the following: Global indicators, Local indicators.

2.5.2.1 Global Indicators of Spatial Autocorrelation

Global statistics summarize the magnitude of spatial autocorrelation for the entire region by a single value. The Global indicators of autocorrelation utilize distance to

define the neighbourhood of a region and measure if and how much the dataset is autocorrelated in the entire study region.

One of the principal global indicator of autocorrelation is the Moran's index I (Moran 1948), defined in formula (2.48)

$$I = \frac{N \sum_i \sum_j w_{ij} (X_i - \bar{X})(X_j - \bar{X})}{(\sum_i \sum_j w_{ij}) \sum_i (X_i - \bar{X})^2} \quad (2.48)$$

where, N is the total pixel number, X_i and X_j are intensity in points i and j (with $i \neq j$), \bar{X} is the average value, w_{ij} is an element of the weight matrix.

$I \in [-1; 1]$; if $I \in [-1; 0)$ there's negative autocorrelation; if $I \in (0; 1]$ there's positive autocorrelation.

Theoretically, if I converges to 0 there's null autocorrelation, in most of the cases, instead of 0, the value used to affirm the presence of null autocorrelation is given by Eq. 2.48:

$$E(I) = -\frac{1}{N-1} \quad (2.49)$$

where N is the number of events in the whole distribution.

The second global indicator of spatial autocorrelation is the Geary's C (Geary 1954), expressed by formula 2.50:

$$C = \frac{(N-1) \sum_i \sum_j w_{ij} (X_i - X_j)^2}{2w_{ij} (\sum_i (X_i - \bar{X})^2)} \quad (2.50)$$

Where symbols have the same meaning than expression 2.48.

$C \in [0; 2]$; if $C \in [0; 1)$ there's positive autocorrelation; if $C \in (0; 2]$ there's negative autocorrelation; if C converges to 1 there's null autocorrelation.

2.5.2.2 Local Indicators of Spatial Autocorrelation

The local version of statistic utilizes distance information to identify local clusters and relies on the distance information captured in Distance matrix. Values indicating the magnitude of spatial association can be derived for each areal unit, namely for each pixel in the case of digital image.

The most common Local indicators of spatial autocorrelation are: Local Moran's I (Anselin 1995), Local Geary's C (Cliff and Ord 1981), and Getis-Ord Local G_i (Getis and Ord 1994; Illian et al. 2008).

Local Moran's I index is defined according to formula 2.51.

$$I_i = \frac{(X_i - \bar{X})}{S_X^2} \sum_{j=1}^N (w_{ij}(X_j - \bar{X})) \quad (2.51)$$

Local Geary's C Index is defined according to formula 2.52.

$$C = \frac{n-1}{\sum_{i=1}^n (X_i - \bar{X})^2} \frac{\sum_{i=1}^n \sum_{j=1}^n w_{ij} (X_i - X_j)^2}{2 \sum_{i=1}^n \sum_{j=1}^n w_{ij}} \quad (2.52)$$

Getis and Ord's Gi is defined according to formula 2.53.

$$G_i(d) = \frac{\sum_{i=1}^n w_i(d)x_i - x_i \sum_{i=1}^n w_i(d)}{S(i) \sqrt{\frac{(N-1) \sum_{i=1}^n w_i(d) - \left(\sum_{i=1}^n w_i(d) \right)^2}{N-2}}} \quad (2.53)$$

These indicators show a different concept of spatial association:

- (1) local Moran's I: a high value of the index means positive correlation both for high values and for low values of intensity;
- (2) Local Geary's C detects areas of dissimilarity between events;
- (3) Getis and Ord's Gi: a high value of the index means positive correlation for high values of intensity, while a low value of the index means positive correlation for low values of intensity.

Such geostatistical analysis tools are available in several commercial softwares, ranging from Geographic Information System (GIS) and image processing ones.

2.5.3 Spatial Autocorrelation Applied to Satellite Data

Spatial autocorrelation examines changes in homogeneity and measures the strength of the relationship between values of the same variables. In the analysis of satellite image it is a very useful tool since it not only considers the value of the pixel (reflectance, temperature, spectral index), but also the relationships between a pixel and its surrounding in a given window size.

Global measures of spatial autocorrelation provide a single value that indicates the level of spatial autocorrelation within the variable distribution, namely the homogeneity of a given values within the image under investigation.

Local measures of spatial autocorrelation provide a value for each location within the variable distribution and, therefore, they are able to identify discrete spatial patterns that may not otherwise be apparent. The statistics output is an image for each calculated index, which contains a measure of autocorrelation around that pixel.

Global and Local statistics can be calculated using spectral channels, spectral combinations and/or multi-temporal combination as intensity.

For all these cases, the first step is to find the optimal lag distance using global Moran's I . It provides different values of lag distances: the optimal value is the lag that maximizes I and captures the autocorrelation of the image in the best way.

At this point, the local indicators of spatial association should be calculated using the optimal lag distance and the selected contiguity.

Results from this assessment must be interpreted and/or further elaborated (generally using classifications) before interpretation. As a general rule, we can argue that the Getis-Ord G_i^* index permits the identification of areas characterized by very high or very low values (hot spots) compared to those of neighboring pixels.

It should be noted that the interpretation of G_i^* is different from that of Moran's I . In detail the Getis-Ord G_i^* enables us to distinguish the clustering of high and low values, but does not capture the presence of negative spatial correlation. It permits the identification of areas characterized by very high or very low values (hot spots) compared to those of neighboring pixels.

The Moran's I is able to detect both positive and negative spatial correlations, but clustering of high or low values are not distinguished. In particular, it identifies pixel clustering. It has values that typically range from approximately +1, representing complete positive spatial autocorrelation, to approximately -1, representing complete negative spatial autocorrelation.

The Local Geary's C index allows us to identify edges and areas characterized by a high variability between a pixel value and its neighboring pixels.

Geostatistical analysis tools are available in several commercial software, such as GIS and image processing (see for example ENVI packages).

References

- Alexakis D, Sarris A, Astaras Th, Albanakis K (2009) Detection of Neolithic settlements in Thessaly (Greece) through multispectral and hyperspectral satellite imagery. *Sensors* 9:1167–1187
- Aminzadeh B, Samani F (2006) Identifying the boundaries of the historical site of Persepolis using remote sensing. *Remote Sens Environ* 102:52–62
- Anselin L (1995) Local Indicators of Spatial Association LISA. *Geogr Anal* 27:93–115
- Beck A (2006) Google earth and world wind: remote sensing for the masses? *Antiquity* 80:308
- Beck A, Philip A, Abdulkarim M, Donoghue D (2007) Evaluation of Corona and Ikonos high resolution satellite imagery for archaeological prospection in western Syria. *Antiquity* 81:161–175
- Bewley R, Donoghue D, Gaffney V, Van Leusen M, Wise A (1999) Archiving aerial photography and remote sensing data: a guide to good practice. Oxbow, Oxford

- Bloisi F, Ebanista C, Falcone L, Vicari L (2010) Infrared image analysis and elaboration for archaeology: the case study of a medieval “capsella” from Cimitile, Italy. *Appl Phys B Laser Opt* 101(1–2):471–479
- Brown Vega M, Craig N, Asencios Lindo G (2011) Ground truthing of remotely identified fortifications on the Central Coast of Perú. *J Archaeol Sci* 38:1680–1689
- Brown CT, Witschey WRT (2003) The fractal geometry of ancient Maya settlement. *J Archaeol Sci* 30:1619–1632
- Burke A, Ebertha D, Cardille J, Dauth D (2008) Paleoethology as a tool for the development of archaeological models of land-use: the Crimean Middle Palaeolithic. *J Archaeol Sci* 35(4):894–904
- Campana S (2003) Ikonos-2 multispectral satellite imagery to the study of archaeological landscapes: an integrated multi-sensor approach in combination with “Traditional” methods. In: *Proceedings of the 30th conference CAA, Heraklion, 2–6 April 2002*, pp 219–225
- Campana S (2004) Le immagini da satellite nell’indagine archeologica: stato dell’arte, casi di studio, prospettive. *Archeologia Aerea. Studi di Aerotopogr Archeol* 1:279–299
- Campana S, Forte M (eds) (2006) From space to place. In: *Proceedings of the 2nd international conference on remote sensing in archaeology, Roma, 4–7 Dec 2006, BAR International Series 1568*. Archaeopress, Oxford
- Campana S, Francovich R (2003) Landscape archaeology in Tuscany: cultural resource management, remotely sensed techniques, GIS based data integration and interpretation. In: *The reconstruction of archaeological landscapes through digital technologies, Boston, 2001, BAR International Series 1151*. Archaeopress, Oxford, pp 15–28
- Ceccato P, Flasse S, Tarantola S, Jacquemoud S, Gregoire JM (2001) Detecting vegetation leaf water content using reflectance in the optical domain. *Remote Sens Environ* 77(1):22–33
- Ceccato P, Flasse S, Gregoire J-M (2002a) Designing a spectral index to estimate vegetation water content from remote sensing data: part 2: validation and applications. *Remote Sens Environ* 82(2–3):198–207
- Ceccato P, Gobron N, Flasse S, Pinty B, Tarantola S (2002b) Designing a spectral index to estimate vegetation water content from remote sensing data: part 1: theoretical approach. *Remote Sens Environ* 82(2–3):188–197
- Chen CM, Hepner GF, Forster RR (2003) Fusion of hyperspectral and radar data using the IHS transformation to enhance urban surface features. *J Photogramm Remote Sens* 58:19–30
- Clark CD, Garrod SM, Parker Pearson M (1998) Landscape archaeology and remote sensing in southern Madagascar. *Int J Remote Sens* 19(8):1461–1477
- Cliff AD, Ord JK (1981) *Spatial processes, models, and applications*. Pion, London
- Crist EP, Cicone RC (1984) A physically-based transformation of thematic mapper data: the TM tasseled cap. *IEEE T Geosci Remote Sens* GE22(33):256–263
- Crist EP, Kauth RJ (1986) The tasseled cap de mystified. *Photogramm Eng Remote Sens* 52(1):81–86
- Daubechies I (1990) The wavelet transform, time–frequency localization and signal analysis. *IEEE Trans Inf Theory* 36(5):961–1005
- Davis CH, Wang X (2003) Planimetric accuracy of Ikonos 1 m panchromatic orthoimage products and their utility for local government GIS basemap applications. *Int J Remote Sens* 24(22):4267–4288
- Deroin J-P, Téreygeol F, Heckes J (2011) Evaluation of very high to medium resolution multi-spectral satellite imagery for geoarchaeology in arid regions – case study from Jabali, Yemen. *J Archaeol Sci* 38:101–114
- Drake NA (1997) Recent aeolian origin of superficial gypsum crusts in Southern Tunisia: geomorphological, archaeological and remote sensing evidence. *Earth Surf Proc Land* 22:641–656
- ENVI (1999) *Users guide, research systems*. Boulder, Colorado
- ERDAS (1999) *Field guide, 5th edn*. ERDAS, Inc., Atlanta

- Estes JE, Jensen JR, Tinney LR (1977) The use of historical photography for mapping archaeological sites. *J Field Archaeol* 4(4):441–447
- Farge M (1992) Wavelet transform and their applications to turbulence. *Ann Rev Fluid Mech* 24:395–457
- Fourty T, Baret F (1998) On spectral estimates of fresh leaf biochemistry. *Int J Remote Sens* 19 (7):1283–1297
- Fowler MJF (1996) High resolution satellite imagery in archaeological application: a Russian satellite photograph of the Stonehenge region. *Antiquity* 70:667–671
- Fritz LW (1996) The era of commercial earth observation satellites. *Photogramm Eng Remote Sens* 62(1):39–45
- Gatrell AC, Bailey TC, Diggle PJ, Rowlingson BS (1996) Spatial point pattern analysis and its application in geographical epidemiology. *Trans Inst Br Geogr* 21:256–271
- Geary RC (1954) The contiguity ratio and statistical mapping. *Inc Stat* 5:115–145
- Getis A, Ord JK (1994) The analysis of spatial association by use of distance statistics. *Geogr Anal* 24:189–206
- Giardino M (2011) A history of NASA remote sensing contributions to archaeology. *J Archaeol Sci* 38:2003–2009
- Gitelson AA, Kaufman Y, Merzlyak MN (1996) Use of green channel in remote sensing of global vegetation from EOS-MODIS. *Remote Sens Environ* 58:289–298
- Grøn O, Palmer S, Stylegar F-A, Aase S, Esbensen K, Kucheryavski S, Sigurd A (2011) Interpretation of archaeological small-scale features in spectral images. *J Archaeol Sci* 38:2024–2030
- Haralick RM, Sternberg SR, Zhuang X (1987) Image analysis using mathematical morphology. *IEEE Trans Pattern Anal Mach Intell* 4:532–550
- Horne JH (2003) A tasselled cap transformation for IKONOS images. In: ASPRS 2003 annual conference proceedings, Anchorage, 5–9 May 2003
- Howey MCL (2011) Multiple pathways across past landscapes: circuit theory as a complementary geospatial method to least cost path for modeling past. *J Archaeol Sci*. doi:[10.1016/j.jas.2011.03.024](https://doi.org/10.1016/j.jas.2011.03.024)
- Huete AR (1988) A soil-adjusted vegetation index (SAVI). *Remote Sens Environ* 25:295–309
- Illian J, Penttinen A, Stoyan H, Stoyan D (2008) Statistical analysis and modelling of spatial point patterns. Wiley, West Sussex, 534 p
- Jackson TJ, Chen D, Cosh M et al (2004) Vegetation water content mapping using Landsat data derived normalized difference water index for corn and soybean. *Remote Sens Environ* 92:475–482
- Kaufman YJ, Tanrer D (1992) Atmospherically resistant vegetation index (ARVI) for EOS-MODIS. *IEEE Geosci Remote Sens* 30:261–270
- Kauth RJ, Thomas GS (1976) The Tasseled cap – a graphical description of the spectral-temporal development of agricultural crops as seen by Landsat. In: Proceedings of the symposium on machine processing of remotely sensed data, Purdue University, West Lafayette, 29 June–1 July 1976, pp 4B41–4B51
- Kennedy D, Bishop MC (2011) Google earth and the archaeology of Saudi Arabia. A case study from the Jeddah area. *J Archaeol Sci* 38:1284–1293
- Kouchoukos N (2001) Satellite images and Near Eastern landscapes. *Near East Archaeol* 64 (1–2):80–91
- Lasaponara R, Masini N (2006a) On the potential of panchromatic and multispectral Quickbird data for archaeological prospection. *Int J Remote Sens* 27:3607–3614
- Lasaponara R, Masini N (2006b) Identification of archaeological buried remains based on Normalized Difference Vegetation Index (NDVI) from Quickbird satellite data. *IEEE Geosci Remote Sens* 3(3):325–328
- Lasaponara R, Masini N (2007a) Detection of archaeological crop marks by using satellite QuickBird multispectral imagery. *J Archaeol Sci* 34:214–221

- Lasaponara R, Masini N (2007b) Improving satellite Quickbird – based identification of landscape archaeological features through tasseled cup transformation and PCA. In: 21st CIPA symposium, Atene, 1–6 giugno 2007
- Lasaponara R, Masini N (2010) Facing the archaeological looting in Peru by local spatial autocorrelation statistics of very high resolution satellite imagery. In: Taniar D et al (eds) Proceedings of ICSSA, the 2010 international conference on computational science and its application, Fukuoka, 23–26 Mar 2010. Springer, Berlin, pp 261–269
- Lasaponara R, Masini N (2011) Satellite remote sensing in archaeology: past, present and future. *J Archaeol Sci* 38:1995–2002
- Lasaponara R, Masini N, Scardozzi G (2008) Satellite based archaeological research in ancient territory of Hierapolis. In: 1st international EARSeL workshop. Advances in remote sensing for archaeology and cultural heritage management, CNR, Rome, 30 Sept–4 Oct 2008. Aracne, Rome, pp 11–16
- Lasaponara R, Masini N, Rizzo E, Coluzzi R, Orefici G (2011) New discoveries in the Piramide Naranjada in Cahuachi (Peru) using satellite, Ground Probing Radar and magnetic investigations. *J Archaeol Sci* 38:2031–2039
- Lillesand TM, Kiefer RW (2000) Remote sensing and image interpretation. Wiley, New York
- Masini N, Lasaponara R (2006) Satellite-based recognition of landscape archaeological features related to ancient human transformation. *J Geophys Eng* 3:230–235. doi:[10.1088/1742-2132/3/3/004](https://doi.org/10.1088/1742-2132/3/3/004)
- Masini N, Lasaponara R (2007) Investigating the spectral capability of QuickBird data to detect archaeological remains buried under vegetated and not vegetated areas. *J Cult Herit* 8(1):53–60
- Miller WC (1957) Uses of aerial photographs in archaeological field work. *Am Antiq* 23(1):46–62
- Moran P (1948) The interpretation of statistical maps. *J R Stat Soc A* 10:243–251
- Murgante B, Las Casas G, Danese M (2008) The periurban city: geo-statistical methods for its definition, Urban and regional data management. Taylor & Francis Group, London, pp 473–485
- Parcak S (2009) Satellite remote sensing for archaeology. Routledge, Abingdon/New York
- Pellemans AH, Jordans RW, Allewijn R (1993) Merging multispectral and panchromatic spot images with respect to the radiometric properties of the sensor. *Photogramm Eng Remote Sens* 59(1):81–87
- Pinty B, Verstraete MM (1992) GEMI: a non-linear index to monitor global vegetation from satellites. *Vegetatio* 101:15–20
- Reeves DM (1936) Aerial photography and archaeology. *Am Antiq* 2(2):102–107
- Richards JA, Jia X (2006) Remote sensing digital image analysis – hardback, 4th edn. Springer, Berlin/Hiedelberg, 476 p
- Sarris A, Jones R (2000) Geophysical and related techniques applied to archaeological survey in the Mediterranean: a review. *J Mediterr Archaeol* 13(1):3–75
- Saunders RW (1990) The determination of broad band surface albedo from AVHRR visible and near-infrared radiances. *Int J Remote Sens* 11:49–67
- Sever TL (1998) Validating prehistoric and current social phenomena upon the landscape of Peten, Guatemala. In: Liverman D, Moran EF, Rinfuss RR, Stern PC (eds) People and pixels: linking remote sensing and social science. National Academy Press, Washington, DC
- Sheets P, Sever T (1988) High tech wizardry. *Archaeology* 41(6):28–35
- Soille P (2003) Morphological image analysis: principles and applications. Springer, Berlin
- Spennemann DHR (1987) Experiences with mapping sites on aerial photographs. *J Field Archaeol* 14(2):255
- Stein C, Cullen B (1994) Satellite imagery and archaeology – a case study from Nikopolis. *Am J Archaeol* 98(2):326
- Stone KH (1964) A guide to the interpretation and analysis of aerial photographs. *Ann Assoc Am Geogr* 54(3):318–328
- Strahler A, Strahler A (1997) Physical geography: science and systems of the human environment. Wiley, New York

- Sussman R, Green G, Sussman I (1994) Satellite imagery, human ecology, anthropology, and deforestation in Madagascar. *Human Ecol* 22(3):333–354
- Telesca L, Coluzzi R, Lasaponara R (2009) Urban pattern morphology time variation in Southern Italy by using Landsat imagery. In: Murgante B, Borruso G, Lapucci A (eds) *Geocomputation & urban planning*, vol SCI 176. Springer, Heidelberg, pp 209–222
- Toutin T (2001) DEM generation from new VIR sensors: IKONOS, ASTER and Landsat-7. In: *IEEE-IGARSS proceedings*, Sydney, 9–13 July 2001
- Toutin T (2002) DEM from stereo Landsat 7 ETM + data over high relief areas. *Int J Remote Sens* 23(10):2133–2139
- Traviglia A (2008) The combinatorial explosion: defining procedures to reduce data redundancy and to validate the results of processed hyperspectral images. In: *Proceedings of the 1st international EARSeL workshop. Advances in remote sensing for archaeology and cultural heritage management*, CNR, Rome, 30 Sept–4 Oct 2008. Aracne, Rome, pp 23–26
- Traviglia A, Cottica D (2011) Remote sensing applications and archaeological research in the Northern Lagoon of Venice: the case of the lost settlement of constanciacus. *J Archaeol Sci* 38:2040–2050
- Treitz PM, Howarth PJ (2000) High spatial resolution remote sensing data for forest ecosystem classification: – an examination of spatial scale. *Remote Sens Environ* 52:268–289
- Tucker CJ (1980) Remote sensing of leaf water content in the near infrared. *Remote Sens Environ* 10:23–32
- Urwin N, Ireland T (1992) Satellite imagery and landscape archaeology: an interim report on the environmental component of the Vinhais Landscape Archaeology Project, North Portugal. *Mediterr Archaeol* 5:121–131
- Ustin SL, Roberts DA, Jacquemoud S, Pinzon J, Gardner M, Scheer GJ, Castaneda CM, Palacios A (1998) Estimating canopy water content of chaparral shrubs using optical methods. *Remote Sens Environ* 65:280–291
- Wang Z, Bovik AC (2002) A universal image quality index. *IEEE Signal Proc Lett* 9(3):81–84
- Wang X-Y, Yang H-Y, Fu Z-K (2010) A new wavelet-based image denoising using undecimated discrete wavelet transform and least squares support vector machine. *Expert Syst Appl* 37(10):7040–7049
- Weber SA, Yool SR (1999) Detection of subsurface archaeological architecture by computer assisted airphoto interpretation. *Geoarchaeology* 14(6):481–493
- Wilson DR (2000) *Air photo interpretation for archaeologists*. Tempus, Stroud
- Zarco-Tejada PJ, Rueda CA, Ustin SL (2003) Water content estimation in vegetation with MODIS reflectance data and model inversion methods. *Remote Sens Environ* 85:109–124
- Zeng P, Dong H, Chi J, Xu X (2004) An approach for wavelet based image enhancement. In: *Proceedings of IEEE international conference on robotics and biomimetics, ROBIO*, Shenyang, 22–26 Aug 2004, pp 574–577
- Zhang H, Bevan A, Fuller D, Fang Y (2010) Archaeobotanical and GIS-based approaches to prehistoric agriculture in the upper Ying valley, Henan, China. *J Archaeol Sci* 37(7): 1480–1489